1-1-2012

The SLUGGS survey: calcium triplet-based spectroscopic metallicites for over 900 globular clusters

C. Usher
Swinburne University of Technology

D. A. Forbes
Swinburne University of Technology

J. P. Brodie
University of California Observatories

C. Foster
European Southern Observatory

L. R. Spitler
Swinburne University of Technology

See next page for additional authors

Recommended Citation

C. Usher, D. A. Forbes, J. P. Brodie, C. Foster, L. R. Spitler, J. A. Arnold, Aaron J. Romanowsky, J. Strader, and V. Pota. "The SLUGGS survey: calcium triplet-based spectroscopic metallicites for over 900 globular clusters" *Monthly Notices of the Royal Astronomical Society* (2012): 1475-1495. https://doi.org/10.1111/j.1365-2966.2012.21801.x

Monthly Notices
of the
ROYAL ASTRONOMICAL SOCIETY

Mon. Not. R. Astron. Soc. **426,** 1475–1495 (2012) doi:10.1111/j.1365-2966.2012.21801.x

The SLUGGS survey: calcium triplet-based spectroscopic metallicities for over 900 globular clusters

Christopher Usher,[1⋆] Duncan A. Forbes,[1] Jean P. Brodie,[2] Caroline Foster,[3] Lee R. Spitler,[1] Jacob A. Arnold,[2] Aaron J. Romanowsky,[2] Jay Strader[4]† and Vincenzo Pota[1]

[1]*Centre for Astrophysics and Supercomputing, Swinburne University of Technology, Hawthorn, VIC 3122, Australia*
[2]*University of California Observatories, 1156 High Street, Santa Cruz, CA 95064, USA*
[3]*European Southern Observatory, Alonso de Cordova 3107, Vitacura, Santiago, Chile*
[4]*Harvard–Smithsonian Centre for Astrophysics, 60 Garden Street, Cambridge, MA 02138, USA*

Accepted 2012 July 26. Received 2012 July 20; in original form 2012 May 25

ABSTRACT

Although the colour distribution of globular clusters in massive galaxies is well known to be bimodal, the spectroscopic metallicity distribution has been measured in only a few galaxies. After redefining the calcium triplet index–metallicity relation, we use our relation to derive the metallicity of 903 globular clusters in 11 early-type galaxies. This is the largest sample of spectroscopic globular cluster metallicities yet assembled. We compare these metallicities with those derived from Lick indices finding good agreement. In six of the eight galaxies with sufficient numbers of high-quality spectra we find bimodality in the spectroscopic metallicity distribution. Our results imply that most massive early-type galaxies have bimodal metallicity as well as colour distributions. This bimodality suggests that most massive early-type galaxies experienced two periods of star formation.

Key words: globular clusters: general – galaxies: abundances – galaxies: star clusters: general – galaxies: stellar content.

1 INTRODUCTION

Optical photometric studies of globular cluster (GC) systems have shown that almost all massive galaxies have bimodal GC colour distributions (e.g. Kundu & Whitmore 2001; Larsen et al. 2001). Since extensive spectroscopy has shown that the majority of GCs are old ($\geq$10 Gyr; e.g. Forbes et al. 2001; Puzia et al. 2005; Strader et al. 2005), this colour bimodality has usually been interpreted as a metallicity bimodality. Metallicity bimodality suggests that each galaxy has experienced two periods of intense star formation (Brodie & Strader 2006) which must be accommodated into any scenario of galaxy formation.

However, both Richtler (2006) and Yoon, Yi & Lee (2006) showed that a strongly non-linear colour–metallicity relation can produce a bimodal colour distribution from a unimodal metallicity distribution. If the slope of the colour–metallicity relation flattens at intermediate colours, small differences in metallicity correspond to large differences in colour creating a gap in the colour distribution where none exists in the metallicity distribution. A unimodal GC metallicity distribution therefore only requires one period of continuous GC formation. Thus the true form of the GC metallicity distribution therefore has important ramifications both for GC formation and for galaxy formation.

Although near-infrared (NIR) photometric studies (e.g. Kundu & Zepf 2007; Spitler, Forbes & Beasley 2008b; Chies-Santos et al. 2012) generally support the interpretation of colour bimodality as metallicity bimodality, large samples of spectroscopic metallicities are required to settle the question of the form of GC metallicity distributions. Unfortunately, only in a few galaxies have a large number of GCs been studied spectroscopically. Although the Milky Way has been long known to host a bimodal metallicity distribution (Harris & Canterna 1979; Zinn 1985), the GC metallicity distribution in M31 is less clear. Barmby et al. (2000) studied the colour and metallicity distribution of M31 GCs. They found colour bimodality in $(V - K)$ but not in $(V - I)$. Using 125 GCs with spectroscopic metallicities they found that the metallicity distribution is bimodal. They showed that given the large reddening and photometric uncertainties, a unimodal colour distribution would be observed from their spectroscopic metallicity distribution about 75 per cent of the time. Using Lick indices, Galleti et al. (2009) derived the metallicities of 245 M31 GCs; they found that the metallicity distribution is either bimodal or trimodal. Caldwell et al. (2011) measured the metallicities of 282 GCs in M31 using the strength of iron spectral indices. Combining their spectroscopic metallicities with 22 GC

⋆E-mail: cusher@astro.swin.edu.au
†Menzel Fellow.

metallicities obtained using resolved colour–magnitude diagrams, they found no statistically significant metallicity bimodality (or trimodality).

Beasley et al. (2008) measured the metallicity of 207 GCs in NGC 5128, the closest, easily observable giant early-type galaxy, using Lick indices, and found a bimodal metallicity distribution. However, the study of Woodley et al. (2010b), which measured the metallicity of 72 GCs in NGC 5128 using Lick indices, did not find statistically significant metallicity bimodality despite finding bimodality in the metallicity sensitive [MgFe]′ index and colour. Alves-Brito et al. (2011) found evidence of metallicity bimodality in a sample of 112 GCs in the early-type spiral M104 (the Sombrero galaxy) which they studied spectroscopically. Cohen, Blakeslee & Ryzhov (1998) determined the metallicities of 150 GCs in M87 using Lick indices and claimed evidence of bimodality. From this data set, Yoon et al. (2006) noted that the metallicity sensitive index Mg *b* had a skewed single-peak distribution rather than a bimodal distribution. Using 47 Lick index measurements by Cohen, Blakeslee & Côté (2003) of the massive elliptical M49's GCs, Strader, Beasley & Brodie (2007) found metallicity bimodality. Although these previous spectroscopic studies suggest that GC metallicity bimodality is common in massive galaxies, a larger galaxy sample is required to confirm it. Due to the large amounts of telescope time required to acquire significant samples of GCs, a more efficient observational technique is required.

The calcium triplet (CaT), at 8498, 8542 and 8662 Å in the rest frame, is one of the strongest spectral features in the optical and NIR. In individual stars the CaT becomes stronger with both increasing metallicity and lower surface gravity (Cenarro et al. 2002). Since giant stars dominate the NIR light of an old population and the surface gravity of metal-rich giants is lower than metal-poor giants, the strength of the CaT in integrated light increases with metallicity. The CaT was first used by Armandroff & Zinn (1988) to measure the metallicities of Milky Way GCs using integrated light and has been successful at determining the metallicities of individual stars (Rutledge, Hesser & Stetson 1997; Battaglia et al. 2008). Single stellar population (SSP) models (Vazdekis et al. 2003, hereafter V03) show that the CaT index of integrated starlight is sensitive to metallicity while being insensitive to ages greater than 3 Gyr. Although the CaT index is only weakly sensitive to the initial mass function (IMF) for the Salpeter (1955) IMF and bottom light IMFs such as the Kroupa (2001) IMF (V03), it is affected by more bottom heavy IMFs such as those found in the most massive elliptical galaxies by van Dokkum & Conroy (2010) and by Cappellari et al. (2012).

Combining a wide-field, red sensitive spectrograph (e.g. the Deep Imaging Multi-Object Spectrograph – DEIMOS; Faber et al. 2003) and the CaT potentially allows large samples of spectroscopic GC metallicities to be assembled. Unfortunately, the CaT has not yet been proven as a reliable metallicity indicator. While Armandroff & Zinn (1988) found a linear relationship between the strength of the CaT and metallicity over the range of metallicity of Milky Way GCs ($-2 <$ [Fe/H] < 0), in the models of V03 the CaT saturates at metallicities greater than [Fe/H] ~ -0.5. Foster et al. (2010, hereafter F10) were the first to use the CaT to determine the metallicity of a large number of extragalactic GCs. They used DEIMOS to measure the metallicities of 144 GCs in NGC 1407. Although they found a bimodal metallicity distribution, the fraction of GCs in the metal-poor peak was different than the fraction of GCs in the blue colour peak. Their measurements of the CaT appeared to be non-linear with colour. They suggested that this conflict is possibly due to saturation of the CaT, a non-linear colour–metallicity relationship or the effects of Paschen lines from hot horizontal branch stars on the CaT measurements. In addition, they found the brightest blue and red GCs to have similar CaT values. More recently, Foster et al. (2011, hereafter F11) used the same technique to study the metallicites of 57 GCs around NGC 4494. Unlike in NGC 1407, NGC 4494 showed a linear relation between colour and the CaT index. Although showing colour bimodality, the CaT strength appeared single peaked in NGC 4494. A larger sample of CaT measurements in multiple galaxies is thus required to establish whether the CaT can be reliably used to measure metallicity of extragalactic GCs.

2 SAMPLE

As part of the ongoing SAGES Legacy Unifying Globulars and Galaxies Survey[1] (SLUGGS; Brodie et al., in preparation), we studied the GC systems of 11 nearby ($D < 30$ Mpc) early-type galaxies. These galaxies cover a range of galaxy masses, morphologies and environments. Details of the galaxies in this study are given in Table 1. Further details of the observations for NGC 3115 were presented in Arnold et al. (2011), for NGC 4494 in F11 and for the remaining galaxies in Pota et al. (2012). We provide summaries of the data acquisition and reduction below.

2.1 Photometry

For most of the galaxies in our sample we used Subaru Suprime-Cam (Miyazaki et al. 2002) *gri* imaging, supplemented with other wide-field imaging and *Hubble Space Telescope* (*HST*) imaging. The sources of our photometry are given in Table 2. We note that the *g*-band imaging in NGC 821 and NGC 5846 and *B*-band imaging from NGC 4278 were observed in poor seeing. All photometry is corrected for the effects of Galactic extinction using the extinction maps of Schlegel et al. (1998). For galaxies and GCs that lack *gri* imaging we used empirical colour conversions to give all GCs equivalent $(g - i)$ colours. These conversions are given in Appendix A. Unlike our spectroscopy, the photometry used in this paper is heterogeneous – it was taken from different studies with different zero-points and aperture corrections. From the wide-field, ground-based imaging we selected GC candidates using cuts in colour–colour space. From *HST* imaging we selected GC candidates using cuts in colour–size space. We refer to the references for each photometric study for details of the selection. Colour–magnitude diagrams and colour histograms of the photometric candidates are shown in Fig. 1.

2.2 Spectroscopy

Between 2006 and 2012, we used DEIMOS on the Keck II telescope in multiobject mode to obtain spectra of large numbers of candidate GCs. These observations were primarily designed to obtain large numbers of GC radial velocities rather than to study GC stellar populations. Early observations used a central wavelength of 7500 Å, while later observations used a central wavelength of 7800 Å. All observations used the 1200 lines mm^{-1} grating and 1 arcsec slits. This set-up yields a resolution of $\Delta\lambda \sim 1.5$ Å and covers the CaT region for almost all slits. We observed two to eleven slit masks per galaxy with typical exposure times of 2 h per mask.

[1] http://sluggs.swin.edu.au

Table 1. Galaxy properties.

Galaxy	Hubble type	V_{sys} (km s^{-1})	$(M-m)$ (mag)	D (Mpc)	M_K (mag)	A_B (mag)	N	$(g-i)$ split	
(1)	(2)	(3)	(4)	(5)	(6)	(7)	(8)	(9)	
NGC 821	E6	1718	31.85	23.4	−24.0	0.48	17	0.97	a
NGC 1400	E0	558	32.14	26.8	−23.9	0.28	34	0.95	b
NGC 1407	E0	1779	32.14	26.8	−25.3	0.30	202	0.98	b
NGC 2768	S0	1353	31.69	21.8	−24.7	0.20	49	0.95	b
NGC 3115	S0	633	29.87	9.4	−24.0	0.21	122	0.93	c
NGC 3377	E6	690	30.19	10.9	−22.8	0.15	84	0.86	b
NGC 4278	E1	620	30.97	15.6	−23.8	0.13	150	0.96	b
NGC 4365	E3	1243	31.84	23.3	−25.2	0.09	131	0.91	b
NGC 4494	E2	1342	31.10	16.6	−24.1	0.09	53	0.99	d
NGC 5846	E0	1712	31.92	24.2	−25.0	0.24	54	0.96	b
NGC 7457	S0	844	30.55	12.9	−22.4	0.23	7	–	e

Column 1: Galaxy name; column 2: Hubble type from the NED data base; column 3: systemic velocity from Cappellari et al. (2011); column 4 ; and column (5): distance modulus and distance from Cappellari et al. (2011) based on surface brightness fluctuations (SBF) of Tonry et al. (2001). For NGC 4365 the SBF distance of Mei et al. (2007) is used. We assume that NGC 1400 and NGC 1407 are parts of the same group and use the mean of their distance moduli. Column 6: K-band absolute magnitude from Cappellari et al. (2011) calculated from the 2MASS (Skrutskie et al. 2006) total K-band apparent magnitude and the distance modulus in column 4, corrected for foreground extinction. Column 7: B-band foreground Galactic extinction from Schlegel, Finkbeiner & Davis (1998). Column 8: number of GCs with CaT measurements. Column 9: $(g-i)$ colour split between subpopulations from literature. NGC 4365 shows evidence for colour trimodality; see Blom, Spitler & Forbes (2012b). NGC 7457 appears unimodal; see Hargis et al. (2011). Colour split references: (a) Spitler et al. (2008a); (b) Pota et al. (2012); (c) this work; (d) F11; (e) Hargis et al. (2011). NGC 1400, NGC 1407 and NGC 3115 are not parts of the Cappellari et al. (2011) study so their radial velocities were taken from NED, while their distances are taken from Tonry et al. (2001) with the same −0.06 mag distance modulus offset. Their K-band absolute magnitude is also calculated from the 2MASS total K apparent magnitude and the distance in column 3.

Table 2. Photometry.

Galaxy	Instrument	Bands	Source
(1)	(2)	(3)	(4)
NGC 821	Suprime-Cam	*gri*	Pota et al. (2012)
NGC 1400	Suprime-Cam	*gri*	Spitler et al. (2012)
NGC 1407	Suprime-Cam	*gri*	Spitler et al. (2012)
NGC 2768	Suprime-Cam	*Riz*	Pota et al. (2012)
	HST ACS	*BVI*	Pota et al. (2012)
NGC 3115	Suprime-Cam	*gri*	Arnold et al. (2011)
NGC 3377	Suprime-Cam	*gri*	Pota et al. (2012)
NGC 4278	Suprime-Cam	*BVI*	Pota et al. (2012)
	HST ACS	*gz*	Pota et al. (2012)
NGC 4365	Suprime-Cam	*gri*	Blom et al. (2012b)
	HST ACS	*gz*	Blom et al. (2012b)
NGC 4494	Suprime-Cam	*gri*	F11
NGC 5846	Suprime-Cam	*gri*	Pota et al. (2012)
	HST WFPC2	*VI*	Forbes, Brodie & Huchra (1996)
NGC 7457	WIYN Minimosaic	*BVR*	Hargis et al. (2011)
	HST WFPC2	*VI*	Chomiuk, Strader & Brodie (2008)

Column 1: Galaxy name; column 2: telescope and instrument; column 3: photometric bands; column 4: reference to source of photometry.

The DEIMOS data were reduced using the IDL SPEC2D pipeline (Cooper et al. 2012; Newman et al. 2012). The pipeline performs flat fielding using internal flats, wavelength calibration using Ar–Kr–Ne–Xe arcs and local sky subtraction. In addition to the science spectrum, a fully propagated error array and a background sky spectrum are also produced by the pipeline for each object. After running the pipeline, heliocentric velocity corrections were applied. Radial velocities were measured using the IRAF[2] procedure FXCOR. To separate GCs from stars Pota et al. (2012) used the friendless algorithm of Merrett et al. (2003) for their galaxies. For NGC 3115 we used a velocity cut of 325 km^{-1} to separate stars and GCs, while in the case of NGC 4494 the GC system is well separated in velocity space from stars. We measured the signal-to-noise ratio (S/N) per Ångstrom of the spectra using the mean S/N per pixel in the range of 8400–8500 Å.

To increase the number of GCs with CaT measurements that have literature metallicities, we supplemented our DEIMOS data with long-slit spectra of two M31 GCs obtained using the Low Resolution Imaging Spectrograph (LRIS) on Keck I (Oke et al. 1995) as poor weather targets on 2010 August 14. These observations used the 600/10 000 grating, a central wavelength of 8448 Å and a 1.5 arcsec slit. B012-G064 was observed for 3 × 300 s, while B225-G280 was observed for 4 × 300 s. These LRIS observations were reduced in the standard manner using IRAF.

2.3 Comparison sample

To compare our CaT metallicities with previous work we assembled a sample of literature metallicities based on Lick indices (Worthey et al. 1994). We used the metallicity studies of Cenarro et al. (2007) for 17 GCs in NGC 1407, Kuntschner et al. (2002) and Norris (private communication) for 14 GCs NGC 3115, Brodie et al. (2005)

[2] IRAF is distributed by the National Optical Astronomy Observatory, which is operated by the Association of Universities for Research in Astronomy (AURA) under cooperative agreement with the National Science Foundation.

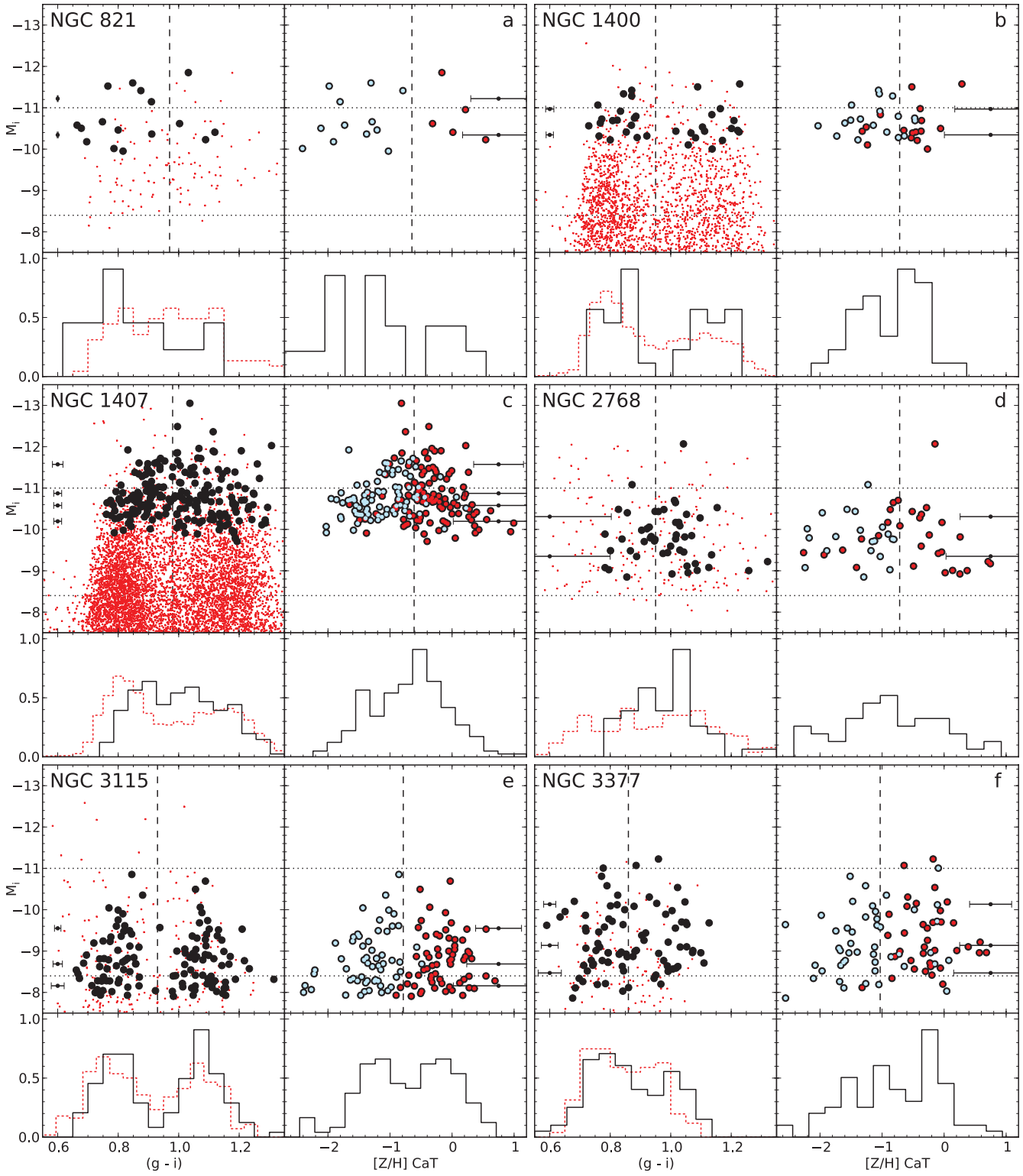

Figure 1. Colour–magnitude and metallicity–magnitude diagrams for each galaxy. For each galaxy the upper left-hand plot is a colour–magnitude diagram, the upper right-hand plot is a CaT metallicity–magnitude diagram, the lower left-hand plot is a normalized colour histogram and the lower right-hand plot is a normalized metallicity histogram. Black filled circles and solid lines are GCs with CaT metallicities; red small points and dotted lines are GC candidates. In the metallicity–magnitude diagrams the centres of the points are colour coded blue or red depending on the photometric colour split. Blue GCs are metal poor; red GCs are metal rich. Median colour and metallicity error bars are plotted to the left and right. The horizontal dashed lines show $M_i = -8.4$, the turnover magnitude from Villegas et al. (2010), and $M_i = -11$, comparable to ω Cen's absolute magnitude ($M_i = -11.25$; Harris 1996) which corresponds to a mass of $\sim 1 \times 10^6\,\mathrm{M}_\odot$. On the colour–magnitude diagrams the vertical dashed line is the colour split between red and blue subpopulations from Table 1. On the metallicity–magnitude diagrams the vertical dashed line is colour split transformed into metallicity using equation (10). Note that the metallicities of blue GCs remain on the metal-poor side of colour division and vice versa.

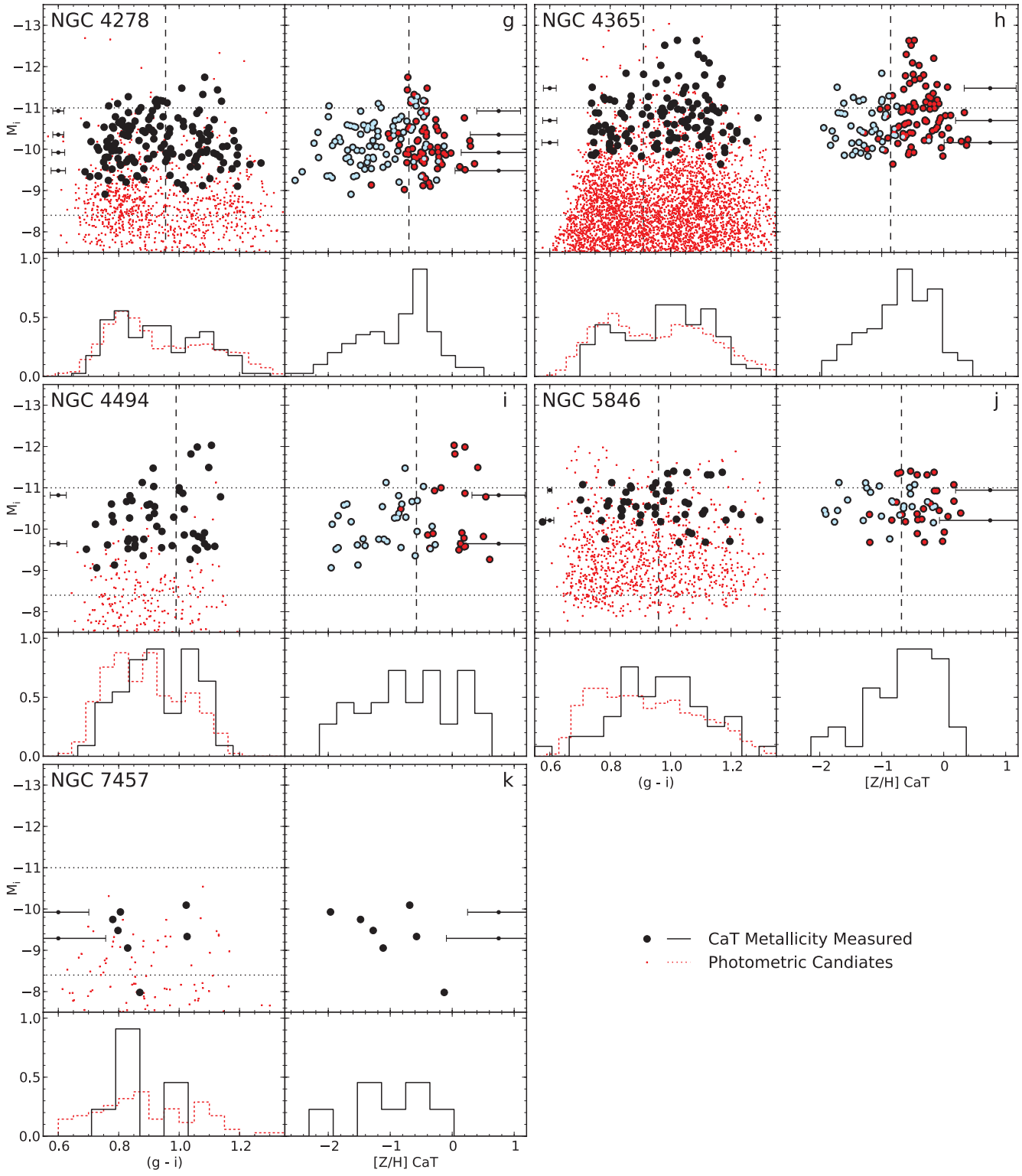

Figure 1 – *continued*

for 21 GCs in NGC 4365 and Chomiuk et al. (2008) for 13 GCs in NGC 7457. All these studies derived metallicities in the same manner using χ^2 minimization of Lick indices with the SSP models of Thomas, Maraston & Bender (2003) and Thomas, Maraston & Korn (2004) (both hereafter TMB03+TMK04). We removed object 25a from Kuntschner et al. (2002) as its colour is much bluer than the other GCs and its radial velocity is low enough to be a galactic star. For these four galaxies we used our own GC photometry.

For M31 we used the metallicities from Caldwell et al. (2011) who used an empirical relationship to derive the metallicities from the strength of Fe Lick indices. Since the Caldwell et al. (2011) metallicities are on the Carretta & Gratton (1997) scale, equation (2)

was used to convert the metallicities to the same TMB03+TMK04 scale used elsewhere in this paper. We used the M31 Sloan Digital Sky Survey (SDSS) GC photometry of Peacock et al. (2010). Due to the variable foreground and internal reddening of M31 we only used the 25 GCs with literature extinction values derived from resolved colour–magnitude diagrams. We used reddening values from Rich et al. (2005), Galleti et al. (2006), Mackey et al. (2007), Perina et al. (2009), Caldwell et al. (2011) and Perina et al. (2011). For GCs in common with multiple studies we used the average value; however, values from other studies were preferred to values from Caldwell et al. (2011). Rich et al. (2005) provides two sets of reddenings: the values adopted and the values fitted as a free parameter. Except for B045-G108 and B311-G033 we used the adopted values; for these two clusters the fitted values provide better agreement with the colour–metallicity trend seen in other clusters. To account for the large uncertainties associated with the reddening correction we have added a 0.05 dex in quadrature to the photometric errors on the colours. In summary we have Lick index-based metallicities for 90 GCs in five galaxies, of which we have measured the CaT strength of 31 GCs.

3 CALCIUM TRIPLET MEASUREMENT

The CaT lies in a region of strong sky lines. Although the DEIMOS pipeline does a good job subtracting the sky, the sky line residuals prevent line indices from being accurately measured directly on the observed spectra. To remove the sky line residuals we used the technique of F10 and fitted stellar templates to the spectra. The stellar templates, which cover a range of metallicities and a range of spectral classes (11 giants and two dwarfs ranging from F to early M), were observed using DEIMOS from 2007 November 12 to 14 using an instrument set-up comparable to the one used for the GCs. The templates were fitted using the PPXF pixel fitting code of Cappellari & Emsellem (2004) which also fits radial velocity, velocity dispersion and continuum shape. We fitted the 8425–8850 Å rest-frame spectral range and masked areas with strong sky lines from the fit.

Before measuring the strength of the CaT on the fitted spectra, the continuum was normalized. Unlike in F10 the continuum was normalized without human intervention. Instead, the continuum was modelled using a linear combination of Chebyshev polynomials of the order of zero to eight. Regions of the fitted spectra around known spectral lines were masked. A continuum model was then fitted using least squares. Pixels more than 0.4 per cent below or 1 per cent above the model were rejected and the model recomputed. This process was repeated until no further pixels were rejected. After the initial fit the pixels were only masked if they deviated from the model. The same index definition (8490.0–8506.0 Å, 8532.0–8552.0 Å and 8653.0–8671.0 Å) as F10 was used to measure the strength of the CaT on the normalized spectra.

In F10 the errors in the measured calcium index were estimated using the S/N of the spectrum. Although the S/N of the spectra dominates the errors, both metallicity and radial velocity do have an effect on the errors. At high metallicities stronger weak metal lines make it harder to fit the continuum while at certain radial velocities such as 200 km s^{-1} CaT lines fall on sky lines. In this work the uncertainties of the index measurements were derived by using a Monte Carlo resampling technique. 100 realizations of the spectra were created from the fitted spectra and the observed error array. The spectral fitting, continuum normalization and index measurement process were repeated for each resampling. The 68th percentiles of the resamplings were used as confidence intervals. This procedure gives asymmetric error bars. After measuring the strength of the CaT and calculating the associated uncertainty, each spectrum was inspected visually to check the results of the automated fitting and normalization. Spectra with large velocity dispersions, $\sigma > 100\,\mathrm{km\,s^{-1}}$, were rejected as likely being contaminated by background galaxy light. Spectra with poor sky subtraction were also rejected. The software used to measure the CaT index and calculate errors is available from the authors upon request.

4 ANALYSIS

4.1 Metallicity scales

Studies of extragalactic GC metallicities have used different metallicity scales. Since they include the effects of varying α element enhancement, the SSP models of TMB03+TMK04 have been commonly used in extragalactic GC studies to derive metallicities from Lick indices. However, studies that have used empirical relations based on the properties of Milky Way GCs tend to use the metallicity values from the Harris (1996) catalogue. Although originally based on the Zinn & West (1984) metallicity scale, the Harris catalogue has evolved with improved abundances and is now based (Harris 2010) on the Carretta et al. (2009) metallicity scale which uses large numbers (∼2000) of high-resolution spectra of individual GC stars. A challenged faced both by SSP models and empirical relations is that the Milky Way lacks the metal-rich GCs seen in massive early-type galaxies.

Since TMB03+TMK04 models have been most commonly used in extragalactic globular stellar population studies, we used their metallicity scale in this paper. To place metallicity measurements and models that used different metallicity scales on the same scale as the one defined by the TMB03+TMK04 models we derived empirical relations using Milky Way GCs. Mendel, Proctor & Forbes (2007) measured stellar population parameters of Milky Way GCs using TMB03+TMK04 models. We used their total metallicities ([Z/H]) and the iron abundances ($[\mathrm{Fe/H}]_{\mathrm{C09}}$) given by Carretta et al. (2009) to derive a linear relationship between the TMB03+TMK04 metallicity scale and the Carretta et al. (2009) iron abundance scale:

$$[\mathrm{Z/H}] = 0.829[\mathrm{Fe/H}]_{\mathrm{C09}} - 0.083\,. \quad (1)$$

This relation has an rms difference of 0.138 dex. We combined the previous relation and the relation provided by Carretta et al. (2009) between their iron abundance scale and the Carretta & Gratton (1997) iron abundance ($[\mathrm{Fe/H}]_{\mathrm{CG97}}$) scale to give a relation between the Carretta & Gratton (1997) iron abundance scale and the TMB03+TMK04 scale:

$$[\mathrm{Z/H}] = 0.943[\mathrm{Fe/H}]_{\mathrm{CG97}} - 0.085\,. \quad (2)$$

This relation has an rms difference of 0.151 dex. We also derived a relation between the TMB03+TMK04 metallicity scale and the scale defined by the 2003 version of the Harris catalogue. Using the Mendel et al. (2007) measurements we found the following relation:

$$[\mathrm{Z/H}] = 0.939[\mathrm{Z/H}]_{\mathrm{H03}} + 0.043\,. \quad (3)$$

This relation has an rms difference of 0.135 dex.

4.2 Biases

Before deriving metallicities we checked whether our CaT measurements were biased by velocity dispersion, radial velocity or S/N. We used V03 SSP model spectra, with an age of 12.6 Gyr and a Kroupa (2001) IMF, to create spectra with arbitrary velocity dispersion, radial velocity and S/N at each of the model metallicities.

The V03 models were used because they well match the resolution of the DEIMOS spectra (∼1.5 Å for both). The V03 models use the isochrones of Girardi et al. (2000) and the empirical stellar library of Cenarro et al. (2001). With increasing velocity dispersion a bias towards lower index values was seen for the highest metallicities. However, this effect only became important for velocity dispersions larger than those seen in GCs. A bias towards higher index values was seen at certain radial velocities such as 200 km s^{-1}. This is likely caused by the CaT lines falling on masked skyline regions. A strong bias to higher index values was seen at S/N $<$ 20 Å^{-1} with the effect being more severe for metal-poor spectra. The bias appears to reverse for the most metal-rich spectra. The difference is seen in the fitted spectra so it is due to the PPXF fitting rather than the normalization process. To correct for this effect the mean CaT value was measured on spectra generated from the model spectra for a range of S/N values and metallicities. By using the mean index values at large (∼300 Å^{-1}) S/N as the true index values, the following relation was used to correct for the S/N bias:

$$\begin{aligned} \mathrm{CaT} &= \mathrm{CaT_{raw}} + a \times (\mathrm{S/N})^b \\ a &= \begin{cases} -22.5\,\mathrm{CaT_{raw}} + 122 & \mathrm{CaT_{raw}} < 4.96 \\ -3.33\,\mathrm{CaT_{raw}} + 27.0 & \mathrm{CaT_{raw}} > 4.96 \end{cases} \\ b &= \begin{cases} -0.343\,\mathrm{CaT_{raw}} + 3.20 & \mathrm{CaT_{raw}} < 5.80 \\ 0.031\,\mathrm{CaT_{raw}} + 1.03 & \mathrm{CaT_{raw}} > 5.80 \end{cases} . \end{aligned} \quad (4)$$

The S/N bias and the applied correction can be seen in Fig. 2. All further CaT values in this study are corrected for the S/N bias. We restrict our analysis to spectra with a S/N greater than 8 Å^{-1}. Using a S/N cut of 10 or 12 Å^{-1} in our analysis gave identical results so we chose to use the lower S/N cut to increase our sample sizes. Colour–magnitude diagrams and colour histograms of the GCs with CaT measurements are shown in Fig. 1.

4.3 Repeated measurements

To assess the quality of the CaT index measurements we compare the 68 repeated measurements in Fig. 3. The reduced χ^2 value of the repeated measurements is 1.41 suggesting that that Monte Carlo resampling process is underestimating the errors. Adding a systematic error of 0.255 Å in quadrature lowers the reduced χ^2 to 1.00 We included this systematic error in future analysis. For repeated objects the simple mean of the CaT indices was used for further analysis.

4.4 Calibration

Two approaches were taken to calibrate the relation between the CaT index and metallicity. First, we used the same approach as F10 using the CaT index strengths of Armandroff & Zinn (1988, hereafter AZ88) to perform an empirical calibration. We derived a relation between our CaT index and the AZ88 index definition ($\mathrm{CaT_{AZ88}}$). We measured both our index and the AZ88 index on V03 SSP models with an age of 12.6 Gyr and a Kroupa (2001) IMF. The following quadratic relation was fitted to the measurements and is shown in Fig. 4 as

$$\begin{aligned} \mathrm{CaT_{AZ88}} &= (-0.068 \pm 0.007)\mathrm{CaT}^2 + (1.55 \pm 0.08)\mathrm{CaT} \\ &\quad + (-0.96 \pm 0.22)\,. \end{aligned} \quad (5)$$

We also rederived the relationship between metallicity and the AZ88 index. Unlike F10 who used the 2003 edition of the Harris (1996) catalogue for metallicities, we used the metallicities provided in appendix A of Carretta et al. (2009) converted to the TMB03+TMK04 scale together with the $\mathrm{CaT_{AZ88}}$ values provided in table 6 of AZ88. Like F10 we ignore highly reddened clusters. Fitting a straight line gives

$$[\mathrm{Z/H}] = (0.54 \pm 0.02)\mathrm{CaT_{AZ88}} + (-3.90 \pm 0.14)\,. \quad (6)$$

This relation is plotted in Fig. 5 and has an rms scatter of 0.11 dex. Combining equations (5) and (6) gives

$$\begin{aligned} [\mathrm{Z/H}] &= (-0.037 \pm 0.004)\mathrm{CaT}^2 + (0.84 \pm 0.06)\mathrm{CaT} \\ &\quad + (-4.42 \pm 0.20), \end{aligned} \quad (7)$$

which is plotted in Fig. 6. This figure gives the relations between our CaT index and metallicity for both of our calibration approaches.

Our second approach to calibrate the relation between metallicity and CaT index was to use the V03 SSP. We measured our index values on the model spectra with an age of 12.6 Gyr and a Kroupa

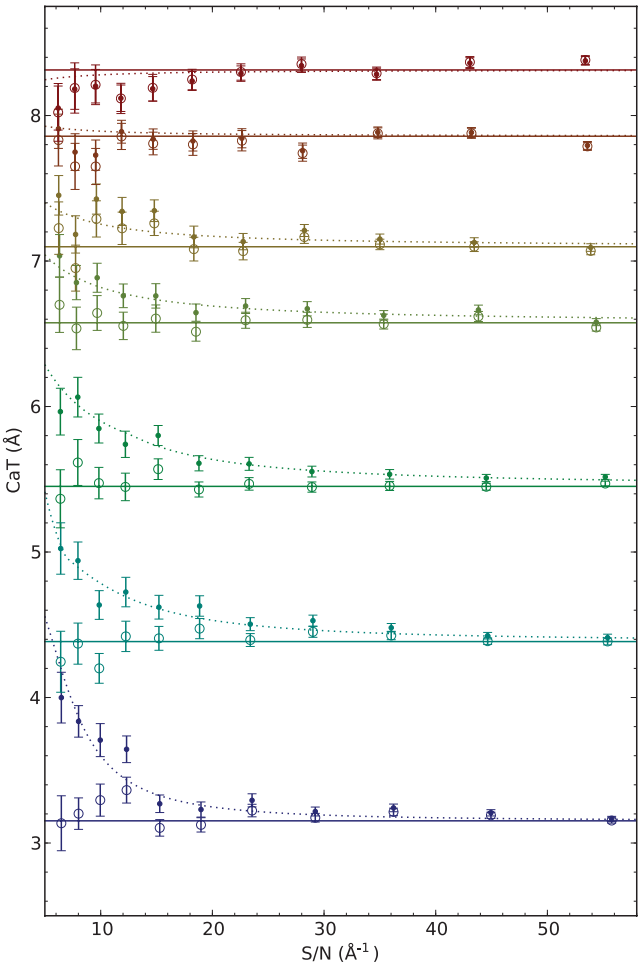

Figure 2. Correction for the S/N bias in the CaT index values. The vertical axis is the CaT index value, and the horizontal axis is the measured S/N. The small points are the mean measured CaT values from spectra generated from Vazdekis et al. (2003) model spectra at different metallicities and S/N values. The solid lines are the CaT values measured at high S/N for each model metallicity. The dotted lines are equation (4), a fit to difference between the measured points and the high-S/N values. The hollow circles show the measured values after using equation (4) to correct them. The colours in this plot scale with the metallicities of the model spectra used with blue being metal poor and red being metal rich. The S/N bias appears to be caused by PPXF.

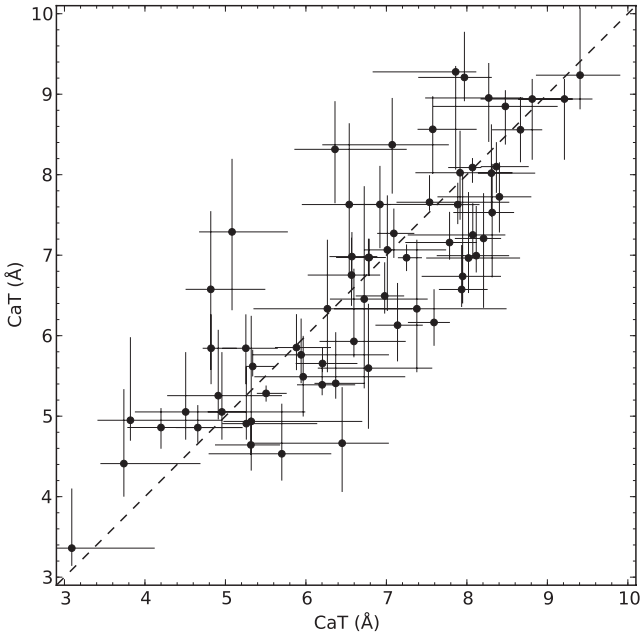

Figure 3. Repeated measurements of CaT index values. The dashed line is one to one. The rms difference of the repeated measurements is 0.84 Å. The error bars include the 0.255 Å systematic error.

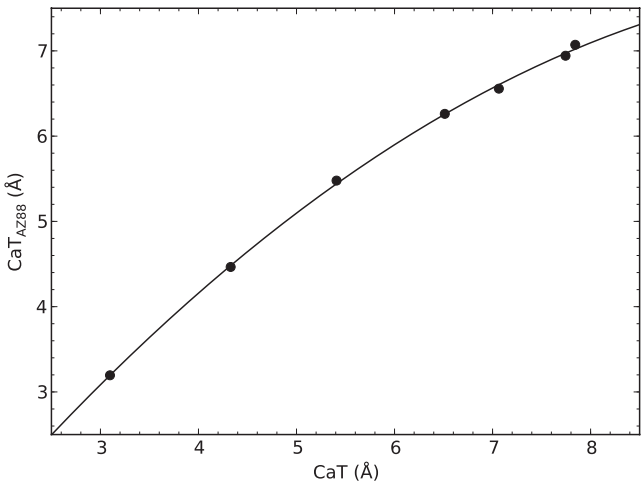

Figure 4. Relation between the CaT index of Armandroff & Zinn (1988) and our index definition. Both indices are measured on spectra from the 12.6 Gyr, Kroupa (2001) IMF, single stellar population models of Vazdekis et al. (2003). The points are the measured values and the solid line is a quadratic fit (equation 5).

(2001) IMF and fitted a linear relation between the metallicity of the models and the measured index value giving a relation of

$$[\mathrm{Z/H}] = (0.461 \pm 0.013)\mathrm{CaT} + (-3.750 \pm 0.080), \quad (8)$$

which is also plotted in Fig. 6. The rms of this relation is 0.048 dex. Unlike TMB03+TMK04, V03 do not correct for the effects of varying [α/Fe] in the local stellar neighbourhood. Following Mendel et al. (2007), we correct the model metallicities for this effect using

$$[\mathrm{Z/H}] = \begin{cases} [\mathrm{Z/H}]_{\mathrm{V03}} & [\mathrm{Z/H}]_{\mathrm{V03}} < -1.0 \\ \dfrac{[\mathrm{Z/H}]_{\mathrm{V03}} - 1.28}{1.28} & -1.0 < [\mathrm{Z/H}]_{\mathrm{V03}} < 0.28 \\ [\mathrm{Z/H}]_{\mathrm{V03}} - 0.28 & 0.28 < [\mathrm{Z/H}]_{\mathrm{V03}} \end{cases}. \quad (9)$$

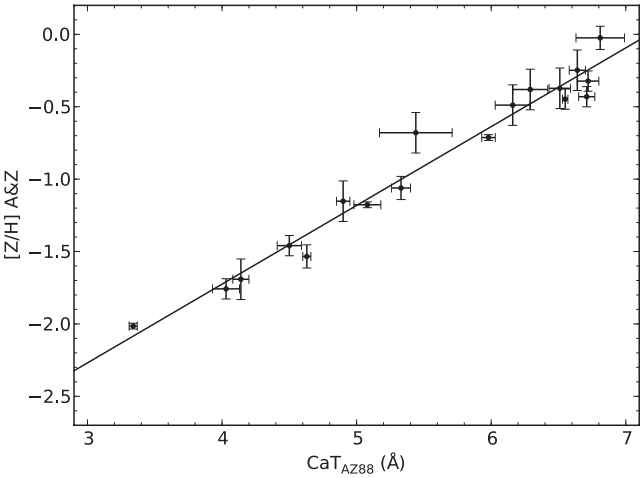

Figure 5. Relation between metallicity ([Z/H]) and the CaT index definition of Armandroff & Zinn (1988) for 18 Milky Way GCs. The [Z/H] values are from Carretta et al. (2009) converted to the same metallicity scale used in the models of Thomas et al. (2003) using equation (1). The solid line is a linear fit (equation 6) which has an rms scatter of 0.11 dex.

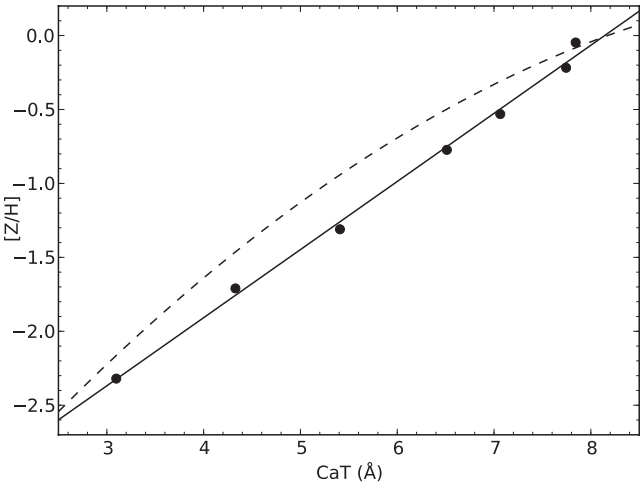

Figure 6. Relation between metallicity ([Z/H]) and our CaT index. The points are the index values measured on the 12.6 Gyr, Kroupa (2001) IMF, single stellar population models of Vazdekis et al. (2003). The model metallicities are corrected for the local stellar α element enhancement pattern using equation (9). The solid line is a linear fit to these points (equation 8). For comparison the dashed line is the relation derived using the measurements of Armandroff & Zinn (1988) (equation 7). Although both calibration techniques agree at high and low metallicities, there is a $\sim$0.3 dex difference in [Z/H] at CaT = 5.5 Å.

To check our results and to choose the better calibration we compared the metallicities we derived with literature spectroscopic measurements. We restricted our analysis to GCs with a S/N greater than 8 Å^{-1} and literature ages greater than 7 Gyr. The comparison of the CaT metallicities derived using the AZ88 empirical calibration with literature metallicities is given in Fig. 7. For most metallicities ([Z/H] < -0.5) this calibration gives metallicities 0.3 dex higher than literature values. However, at higher metallicities there is good agreement.

The comparison of the CaT metallicities derived using the V03 SSP models with literature metallicities is also given in Fig. 7. Unlike the empirical calibration, the SSP-based calibration approach gives metallicities in good agreement with literature values across

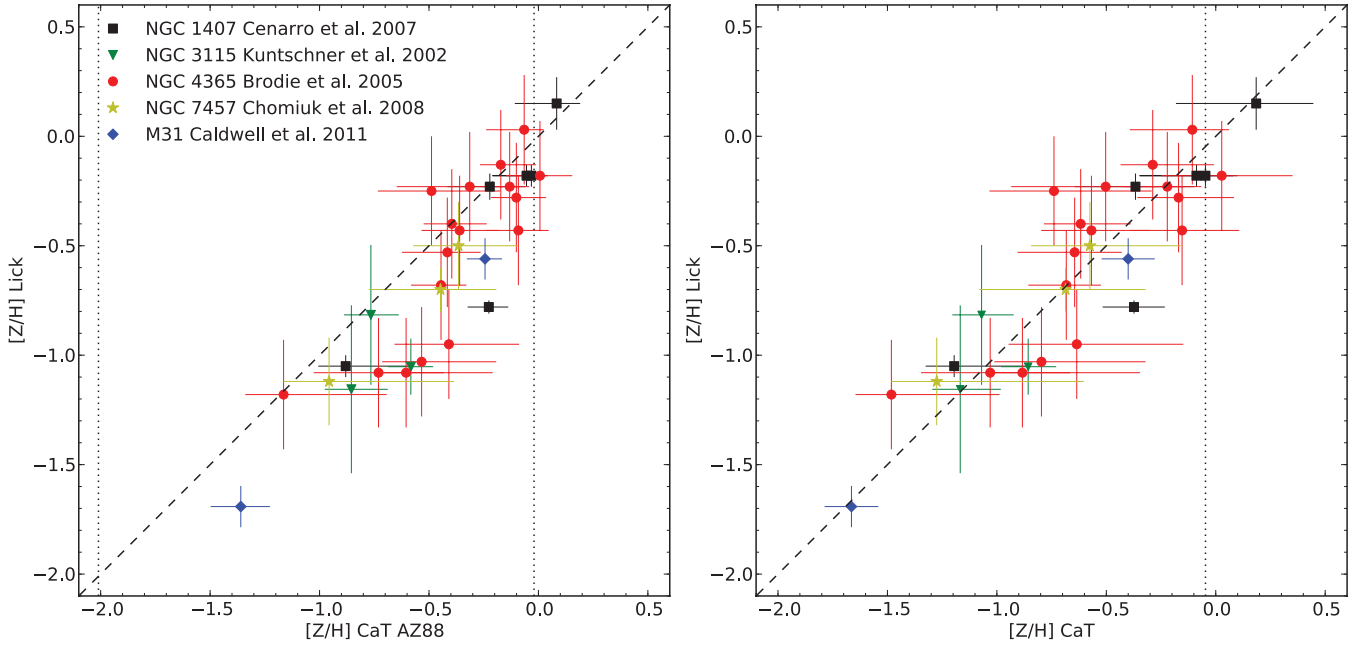

Figure 7. Left: CaT metallicities derived using Armandroff & Zinn (1988) based calibration compared to literature Lick index-based metallicities. Different galaxies and studies are denoted by different colours and symbols. The dashed line is one to one and the vertical dotted lines correspond to the highest ([Z/H] = −0.02) and lowest ([Z/H] = −2.02) metallicity Galactic GCs used to derive the relation between index strength and metallicity. For metallicities of [Z/H] < −0.5, the metallicities given by empirical calibration are about 0.3 dex higher than the literature values. The rms scatter is 0.27 dex and the reduced χ^2 value is 2.26. Right: CaT metallicities derived using single stellar population (SSP) model of Vazdekis et al. (2003) compared to literature metallicities. Different galaxies and studies are denoted by different colours and symbols. The dashed line is one to one, while the vertical dotted line corresponds to the highest metallicity SSP model ([Z/H] = −0.05) used to derive the relation between index strength and metallicity. The lowest metallicity SSP population model used ([Z/H] = −2.32) is too low to appear on this plot. The rms scatter is 0.20 dex and the reduced χ^2 value is 0.59.

Table 3. Calcium triplet measurements and metallicities.

Name	RA	Dec.	$(g-i)$	i	CaT	[Z/H]
	(°)	(°)	(mag)	(mag)	(Å)	(dex)
(1)	(2)	(3)	(4)	(5)	(6)	(7)
NGC4494_GC100	187.811375	25.779614	0.93 ± 0.03	21.04 ± 0.02	$7.44^{+0.54}_{-0.64}$	$-0.32^{+0.25}_{-0.29}$
NGC4494_GC101	187.855092	25.783281	0.98 ± 0.08	20.81 ± 0.06	$6.52^{+1.47}_{-0.54}$	$-0.75^{+0.68}_{-0.25}$
NGC4494_GC102	187.873400	25.783786	1.04 ± 0.03	21.84 ± 0.02	$9.46^{+0.64}_{-0.94}$	$0.60^{+0.30}_{-0.43}$
...	...	...	...	...	...	...

This table is available in its entirety in the online journal (see Supporting Information). Column 1: globular cluster (GC) IDs. The IDs are the same as in Pota et al. (2012) except for the GCs in NGC 4494, where 'NGC4494_' has been appended to the IDs from F11. Columns 2 and 3: right ascension and declination in the J2000.0 epoch, respectively; column 4: adopted $(g-i)$ colour; column 5: adopted i magnitude; column 6: CaT index measurement corrected for S/N bias; column 7: total metallicity.

the whole range of observed metallicities. Since the reduced χ^2 value is significantly lower for the SSP calibration (0.59) than for the empirical calibration (2.26) and gives better qualitative agreement, we choose to use the SSP calibration approach for the rest of the analysis (except when comparing to the previous measurements of F10 and F11 in Section 5.4). Metallicity–magnitude diagrams and metallicity histograms for each galaxy are plotted in Fig. 1. Colours, magnitudes, CaT index measurements and CaT metallicities for all measured GCs are given in Table 3 which is available in its entirety online (see Supporting Information).

4.5 Colour–metallicity relation

To compare the colours of GCs with their CaT metallicities we constructed an empirical colour–metallicity relation using literature metallicities (Section 2.3) and our own photometry. We fitted the following broken linear function (see Fig. 8):

$$[\mathrm{Z/H}] = \begin{cases} (7.46 \pm 1.28) \times (g-i) + (-7.09 \pm 1.01) \\ \qquad\qquad (g-i) < 0.77 \\ (3.49 \pm 0.12) \times (g-i) + (-4.03 \pm 0.11) \\ \qquad\qquad (g-i) > 0.77 \end{cases}. \quad (10)$$

The rms of this colour–metallicity relation is 0.17 dex. Versions of this relation in other optical colours are available in Appendix B. Combining colour–metallicity data from multiple galaxies may introduce scatter due to variations in the photometric zero-points and reddening corrections. We note that the break in the colour–metallicity relation occurs at roughly the same metallicity

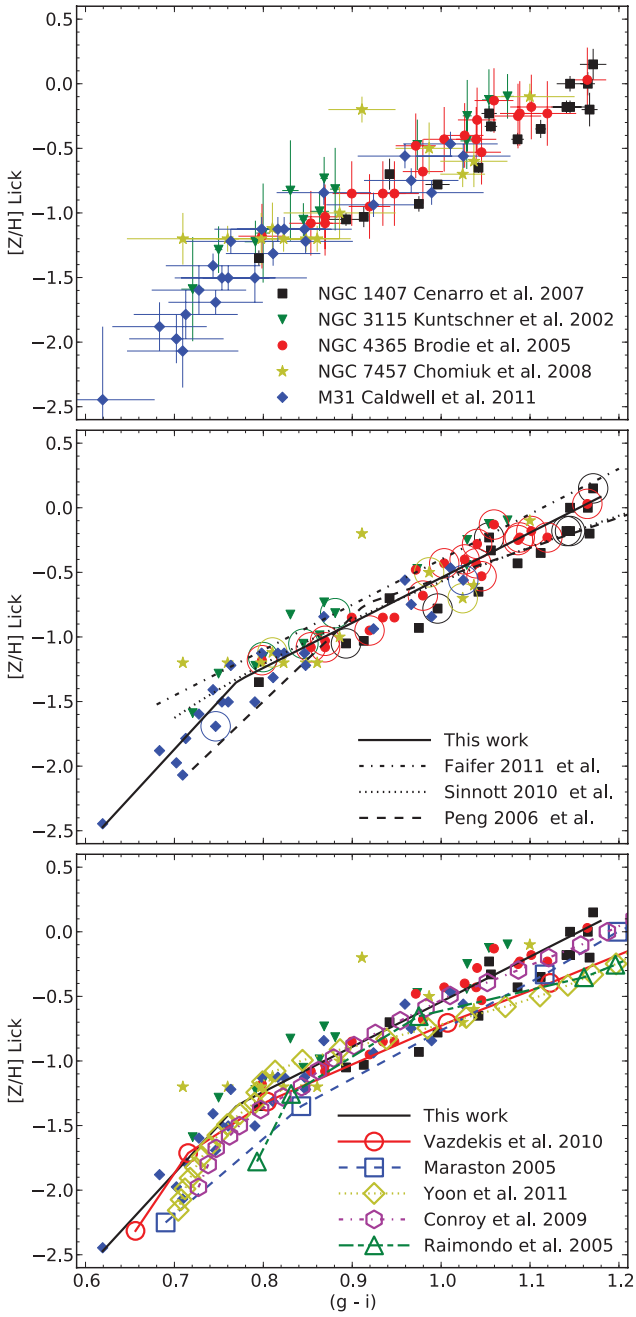

Figure 8. Globular cluster colour–metallicity relations. Note that different studies used different techniques to derive metallicities and colours (see text for details) although we attempt place them on the same scales. Top: different colours and symbols refer to different galaxy studies. For [Z/H] > -1.4 the colour appears to be linear, while for [Z/H] < -1.4 the relation steepens. Middle: empirical colour–metallicity relations. The solid line is our broken linear fit to the data, while the other lines are the colour–metallicity relations of Faifer et al. (2011), Sinnott et al. (2010) and Peng et al. (2006). The different relations agree within the uncertainties of each relation above $(g - i) \sim 0.8$. We have measured CaT metallicities for the circled points. Bottom: single stellar population (SSP) model colour–metallicity relations. The solid line is our broken linear fit to the data. The coloured lines are the SSP models of Vazdekis et al. (2010), Maraston (2005), Yoon et al. (2011), Conroy, Gunn & White (2009) and Raimondo et al. (2005). All models are ∼13 Gyr old; see text for details of the other stellar population parameters used.

([Z/H] ~ -1.4) as the break in the metallicity–iron index relation used by Caldwell et al. (2011).

A comparison of the metallicity distribution derived from the CaT compared to the distribution derived from the colours is given by the cumulative histograms in Fig. 9. To quantify this comparison we ran the Kolmogorov–Smirnov (KS) test on the CaT metallicities and the colour-based metallicities for the same objects. A non-parametric test, the KS test measures the probability that two samples are drawn from the same distribution. We take a probability of less than $p = 0.05$ as evidence that the CaT-based and colour-based metallicities are drawn from different distributions and inconsistent with one another. The results of the KS tests are given in Fig. 9.

4.6 Testing bimodality

To test for colour and metallicity bimodality we used the Gaussian mixture modelling (GMM) code of Muratov & Gnedin (2010). An improved version of the widely used KMM code of Ashman, Bird & Zepf (1994), GMM calculates both the best-fitting unimodal and best-fitting bimodal distributions to the data. It then runs a parametric bootstrap to determine whether the bimodal distribution is preferred. Muratov & Gnedin (2010) discuss detecting bimodality and note that looking for an improved fit by two Gaussians over one is not so much a test of bimodality as a test of non-Gaussianity. Therefore further requirements must be met to declare a population bimodal. Muratov & Gnedin (2010) suggest using the relative separation of the fitted peaks, D, and the kurtosis of the sample to decide whether a sample is bimodal. They require $D > 2$ and negative kurtosis in addition to a significant bootstrap test result for a population to be bimodal. We adopt the same requirements. In line with previous bimodality studies we consider a distribution bimodal if bimodality is preferred over unimodality with a probability of $p \geq 0.9$.

In addition to running GMM on the colours and metallicities (both colour-based and CaT-based) of the GCs with CaT measurements, we ran GMM on the colours of the GC photometric candidates. The photometric candidates were restricted to those in the absolute magnitude range $-13.5 < M_i < -8.4$, the fainter limit corresponding to the turnover magnitude (Villegas et al. 2010) which is the peak of the GC magnitude distribution. We also limited the galactocentric radial range to radii less than that of the most distant spectroscopically confirmed GC. In the case of NGC 4494 we followed F11 and excluded candidates closer than 0.5 arcmin to the galaxy. We did not make any corrections for contamination; such corrections would be different in each galaxy. We only ran GMM when the sample size was greater than or equal to 40. Results of running GMM on the metallicity distributions are given in Table 4 and on the colours in Table 5. The GMM metallicity results are plotted in Fig. 10.

5 DISCUSSION

5.1 The calcium triplet as a metallicity indicator

Fig. 7 shows that metallicities measured using the CaT calibrated with SSP models agree with metallicities measured using traditional Lick analysis better than the empirical, AZ88-based, calibration. The agreement is seen over the range of observed metallicities and over a range of both GC magnitudes and galaxy masses. Since the CaT technique relies on the strength of a single spectral feature, using the CaT to determine metallicities assumes that the age–metallicity, metallicity–calcium abundance and metallicity–horizontal branch morphology relationships are the same for all GCs in all galaxies as well as the same IMF. The CaT shares this

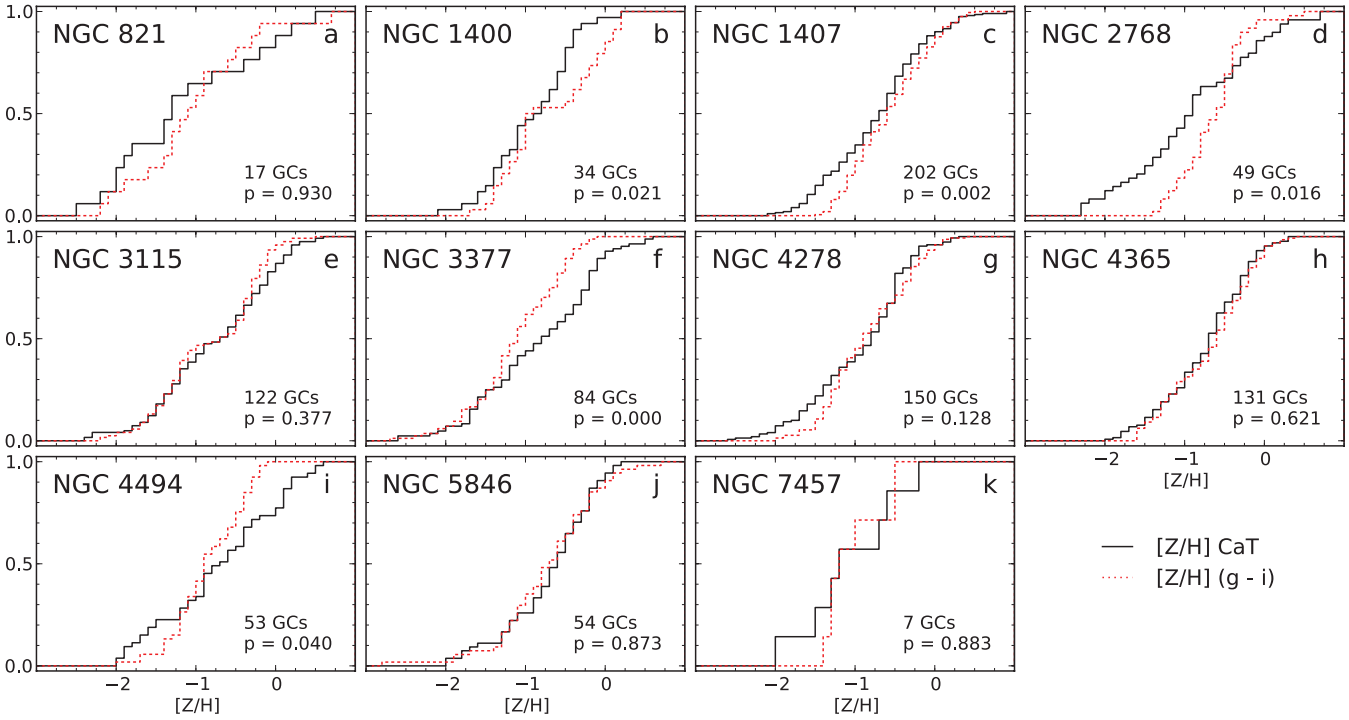

Figure 9. Cumulative metallicity histograms for each galaxy. The solid black lines are the metallicities derived using the CaT; the dashed red lines are the same GCs with metallicities derived using $(g - i)$ colours. The probability given by the KS test that the two samples are drawn from the same distribution is given in the lower right-hand corner of each plot along with the number of GCs with CaT measurements.

issue with using colours or indices such the [MgFe]′ index (Thomas et al. 2003) to derive metallicities.

Unlike V03 we do not see that the CaT saturates with metallicity, at least for metallicities up to solar. We speculate that this is due to the effect of weak metal lines, some of which lie in the continuum passbands of the CaT indices of AZ88 and Cenarro et al. (2001), acting to lower the pseudo-continuum of the CaT at high metallicities. Since the strength of the CaT increases and the pseudo-continuum decreases with metallicity, these indices saturate at high metallicity. As our technique fits the continuum, avoiding regions with weak metal lines, our continuum is less effected and our index does not saturate.

5.2 The colour–metallicity relation of globular clusters

In Fig. 8 we compared our empirical colour–metallicity relationship (equation 10) to those from literature (middle panel) and to a range of different SSP models (lower panel). Comparing different relations is complicated due to the different metallicity scales used by various authors. We compared the following empirical relations.

(i) *The Faifer et al. (2011) relation* was based on GMOS photometry and spectroscopy of GCs in NGC 3379, NGC 3923 and NGC 4649. The metallicities were derived using χ^2 minimization of Lick indices and the models of TMB03+TMK04.

(ii) *The Sinnott et al. (2010) relation* used photometry of NGC 5128 obtained using the Y4KCam imager on the Cerro Tololo Inter-American Observatory/Yale 1.0-m telescope and metallicities derived using the strength of the [MgFe]′ index calibrated to Milky Way GCs tied to the Harris metallicity scale. This relation was converted to the TMB03+TMK04 metallicity scale using equation (3).

(iii) *The Peng et al. (2006) relation* used Advanced Camera for Surveys (ACS) and SDSS photometry of M49 and M87 GCs together with unpublished photometry of Milky Way GCs. Metallicities for M49 (Cohen et al. 2003) and M87 (Cohen et al. 1998) were derived using the models of Worthey (1994) and a limited number of Lick indices, while Milky Way metallicities came from the Harris (1996) catalogue. The Peng et al. relation was converted from $(g - z)$ to $(g - i)$ using equation (A1) and from the Harris metallicity scale to our metallicity scale using equation (3).

Although they disagree below $(g - i) \sim 0.8$, all three relations agree with our empirical colour–metallicity relations within the uncertainties of each relation.

We also compared our empirical colour–metallicity relation with the SSP models of Vazdekis et al. (2010), Maraston (2005), Yoon et al. (2011), Conroy et al. (2009) and Raimondo et al. (2005). We choose to compare the models at the same age (∼13 Gyr). The metallicity scale of the models is closer to the metallicity scale of Carretta et al. (2009) than the TMB03+TMK04 used in this paper so we used equation (1) to convert the model metallicities to the scale of TMB03+TMK04. Below we briefly describe each set of models.

(i) *Version 9.1 of the SSP models of Vazdekis et al. (2010).* We choose models with a Kroupa (2001) IMF and with an age of 12.6 Gyr. Since these models only provide predictions in Johnson–Cousins filters, we use the transformation of Jordi, Grebel & Ammon (2006) to convert $(V - I)$ to $(g - i)$. For the most metal-poor GCs these models predict colours that are too blue while for metal-rich GCs they predict colours that are too red.

(ii) *The Maraston (2005) SSP models.* We choose models with a Kroupa (2001) IMF and with an age of 13 Gyr. The Maraston models give a choice of blue or red horizontal branches at low metallicities; we choose the blue models as they provide better agreement with the data. Except for the most metal-poor GCs these models predict redder colours at a given metallicity than most of the observed GCs.

Table 4. Bimodal metallicity distribution results using GMM.

Galaxy (1)	Sample (2)	N (3)	$\mu_{\rm poor}$ (4)	$\sigma_{\rm poor}$ (5)	$\mu_{\rm rich}$ (6)	$\sigma_{\rm rich}$ (7)	$f_{\rm poor}$ (8)	p (9)	D (10)	k (11)	Bi (12)
NGC 1407	$(g-i)$	202	-1.01 ± 0.08	0.19 ± 0.04	-0.27 ± 0.10	0.38 ± 0.05	0.34 ± 0.11	0.999	2.50 ± 0.28	-0.96	Y
	CaT	202	-1.52 ± 0.26	0.23 ± 0.12	-0.53 ± 0.36	0.52 ± 0.11	0.16 ± 0.22	0.946	2.46 ± 0.66	-0.40	Y
NGC 2768	$(g-i)$	49	-0.64 ± 0.28	0.34 ± 0.10	0.48 ± 0.48	0.11 ± 0.14	0.96 ± 0.36	0.645	4.40 ± 1.51	0.37	N
	CaT	49	-1.12 ± 0.44	0.64 ± 0.20	0.07 ± 0.43	0.40 ± 0.17	0.78 ± 0.29	0.141	2.24 ± 0.68	-0.78	N
NGC 3115	$(g-i)$	122	-1.33 ± 0.04	0.32 ± 0.04	-0.23 ± 0.03	0.23 ± 0.03	0.49 ± 0.05	0.999	3.94 ± 0.37	-1.06	Y
	CaT	122	-1.19 ± 0.10	0.50 ± 0.09	-0.07 ± 0.06	0.32 ± 0.05	0.57 ± 0.08	0.998	2.67 ± 0.50	-0.75	Y
NGC 3377	$(g-i)$	84	-1.24 ± 0.41	0.49 ± 0.12	-0.45 ± 0.24	0.16 ± 0.12	0.80 ± 0.27	0.903	2.13 ± 0.72	-0.22	Y
	CaT	84	-1.29 ± 0.29	0.54 ± 0.15	-0.16 ± 0.15	0.35 ± 0.12	0.56 ± 0.17	0.910	2.49 ± 0.62	-0.66	Y
NGC 4278	$(g-i)$	150	-1.08 ± 0.07	0.34 ± 0.05	-0.22 ± 0.08	0.25 ± 0.05	0.66 ± 0.09	0.995	2.86 ± 0.37	-0.82	Y
	CaT	150	-1.48 ± 0.15	0.42 ± 0.09	-0.48 ± 0.05	0.32 ± 0.06	0.41 ± 0.11	0.999	2.65 ± 0.53	-0.47	Y
NGC 4365	$(g-i)$	131	-1.26 ± 0.07	0.21 ± 0.04	-0.36 ± 0.06	0.33 ± 0.04	0.30 ± 0.06	0.999	3.26 ± 0.31	-0.97	Y
	CaT	131	-1.47 ± 0.23	0.25 ± 0.10	-0.51 ± 0.12	0.40 ± 0.07	0.18 ± 0.16	0.951	2.88 ± 0.53	-0.58	Y
NGC 4494	$(g-i)$	53	-0.99 ± 0.18	0.35 ± 0.08	-0.31 ± 0.12	0.13 ± 0.05	0.71 ± 0.16	0.954	2.55 ± 0.67	-0.58	Y
	CaT	53	-0.90 ± 0.38	0.62 ± 0.19	0.26 ± 0.32	0.19 ± 0.17	0.80 ± 0.27	0.819	2.51 ± 0.53	-1.08	N
NGC 5846	$(g-i)$	54	-2.79 ± 0.91	0.14 ± 0.32	-0.63 ± 0.33	0.55 ± 0.16	0.02 ± 0.30	0.841	5.37 ± 2.20	1.19	N
	CaT	54	-1.42 ± 0.31	0.35 ± 0.14	-0.41 ± 0.13	0.34 ± 0.08	0.24 ± 0.18	0.925	2.93 ± 0.99	-0.43	Y

Column 1: Galaxy name; column 2: colour or CaT-based metallicity; column 3: number of GCs with CaT measured; column 4: mean metallicity of the metal-poor subpopulation; column 5: dispersion of the metal-poor subpopulation; column 6: mean metallicity of the metal-rich subpopulation; column 7: dispersion of the metal-rich subpopulation; column 8: fraction of the clusters in the metal-poor population; column 9: p-value that a bimodal fit is preferred over a unimodal fit; column 10: separation of the GMM peaks normalized by their width; column 11: the kurtosis of the sample; column 12: bimodality of the sample. A p-value greater than 0.9, a separation of $D > 2$ and a negative kurtosis are all required for a sample to be considered bimodal. We did not run GMM on NGC 821 (17 GCs), NGC 1400 (34 GCs) and NGC 7457 (seven GCs) due to the low number of GCs with CaT measurements in these galaxies.

Table 5. Bimodal colour distribution results using GMM.

Galaxy (1)	Sample (2)	N (3)	$\mu_{\rm blue}$ (4)	$\sigma_{\rm blue}$ (5)	$\mu_{\rm red}$ (6)	$\sigma_{\rm red}$ (7)	$f_{\rm blue}$ (8)	p (9)	D (10)	k (11)	Bi (12)
NGC 821	All	110	0.81 ± 0.05	0.04 ± 0.03	1.03 ± 0.10	0.16 ± 0.04	0.18 ± 0.26	0.969	1.87 ± 0.70	-0.48	N
NGC 1400	All	1010	0.80 ± 0.01	0.06 ± 0.01	1.09 ± 0.02	0.10 ± 0.01	0.53 ± 0.05	0.990	3.53 ± 0.37	-1.16	Y
NGC 1407	All	3312	0.82 ± 0.00	0.06 ± 0.00	1.12 ± 0.01	0.11 ± 0.01	0.48 ± 0.02	0.990	3.36 ± 0.12	-1.13	Y
	CaT	202	0.86 ± 0.02	0.05 ± 0.01	1.08 ± 0.03	0.11 ± 0.01	0.34 ± 0.11	0.999	2.50 ± 0.27	-0.97	Y
NGC 2768	All	195	0.70 ± 0.04	0.05 ± 0.02	1.00 ± 0.03	0.16 ± 0.01	0.17 ± 0.09	0.999	2.51 ± 0.23	-0.78	Y
	CaT	49	0.97 ± 0.08	0.10 ± 0.03	1.29 ± 0.14	0.03 ± 0.04	0.96 ± 0.36	0.645	4.40 ± 1.51	0.37	N
NGC 3115	All	180	0.77 ± 0.01	0.09 ± 0.01	1.07 ± 0.01	0.07 ± 0.01	0.54 ± 0.04	0.999	3.88 ± 0.26	-1.24	Y
	CaT	122	0.79 ± 0.01	0.06 ± 0.01	1.09 ± 0.01	0.07 ± 0.01	0.47 ± 0.05	0.999	4.74 ± 0.39	-1.38	Y
NGC 3377	All	71	0.75 ± 0.02	0.05 ± 0.02	0.94 ± 0.03	0.07 ± 0.02	0.52 ± 0.13	0.997	3.07 ± 0.54	-1.02	Y
	CaT	84	0.79 ± 0.02	0.08 ± 0.01	1.01 ± 0.03	0.06 ± 0.01	0.67 ± 0.10	0.994	3.32 ± 0.46	-1.01	Y
NGC 4278	All	700	0.82 ± 0.01	0.08 ± 0.01	1.10 ± 0.01	0.10 ± 0.01	0.63 ± 0.03	0.999	3.28 ± 0.20	-0.82	Y
	CaT	150	0.80 ± 0.03	0.05 ± 0.02	1.02 ± 0.04	0.11 ± 0.02	0.40 ± 0.13	0.999	2.56 ± 0.49	-1.02	Y
NGC 4365	All	2159	0.79 ± 0.00	0.06 ± 0.00	1.05 ± 0.01	0.12 ± 0.00	0.36 ± 0.02	0.990	2.82 ± 0.10	-1.01	Y
	CaT	131	0.80 ± 0.01	0.04 ± 0.01	1.05 ± 0.01	0.10 ± 0.01	0.28 ± 0.06	0.999	3.34 ± 0.31	-1.08	Y
NGC 4494	All	127	0.86 ± 0.02	0.09 ± 0.01	1.07 ± 0.03	0.03 ± 0.01	0.80 ± 0.09	0.999	3.07 ± 0.32	-0.97	Y
	CaT	53	0.86 ± 0.02	0.08 ± 0.01	1.06 ± 0.02	0.04 ± 0.01	0.65 ± 0.11	0.986	3.20 ± 0.53	-1.14	Y
NGC 5846	All	894	0.76 ± 0.02	0.07 ± 0.01	1.01 ± 0.02	0.14 ± 0.01	0.34 ± 0.08	0.999	2.29 ± 0.16	-0.89	Y
	CaT	54	0.89 ± 0.09	0.13 ± 0.05	1.05 ± 0.13	0.14 ± 0.05	0.50 ± 0.30	0.022	1.18 ± 1.14	-0.24	N
NGC 7457	All	46	0.85 ± 0.04	0.17 ± 0.05	1.43 ± 0.18	0.04 ± 0.08	0.98 ± 0.22	0.551	4.70 ± 1.49	0.44	N

Column 1: Galaxy name; column 2: whether all GC candidates or just GCs with CaT measurements; column 3: number of GCs; column 4: mean colour of the blue subpopulation; column 5: dispersion of the blue subpopulation; column 6: mean colour of the red subpopulation; column 7: dispersion of the red subpopulation; column 8: fraction of the clusters in the blue population; column 9: p-value that a bimodal fit is preferred over a unimodal fit; column 10: separation of the GMM peaks normalized by their width. Column 11: the kurtosis of the sample; column 12: bimodality of the sample. A p-value greater than 0.9, a separation of $D > 2$ and a negative kurtosis are all required for a sample to be considered bimodal.

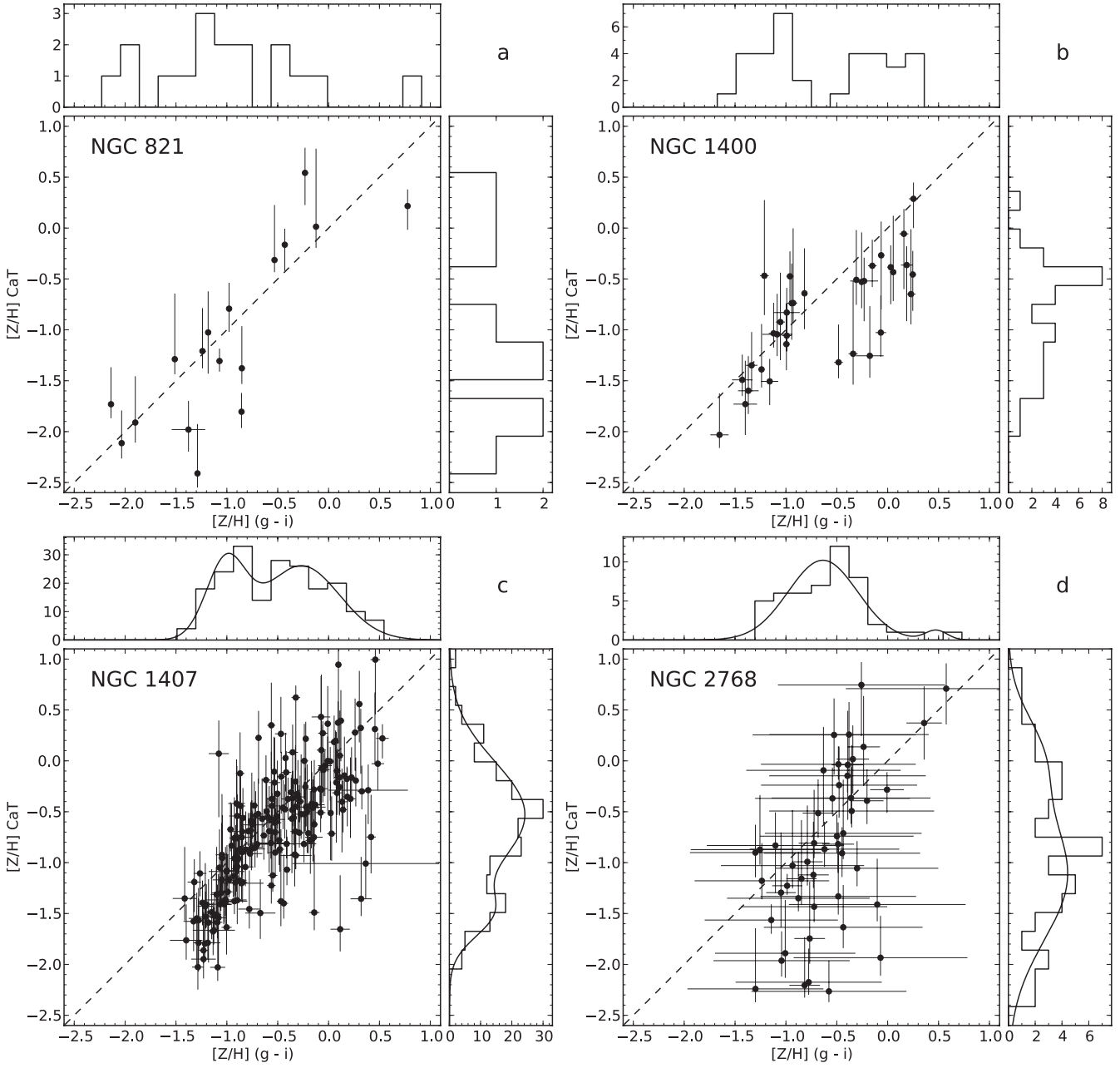

Figure 10. Comparison of colour-based and CaT-based metallicities for each galaxy. On the vertical axis is the CaT-based metallicity; on the horizontal axis is colour-based metallicity. The plots on top are the colour-based metallicity histograms; to the right are the CaT-based metallicity histograms. The bimodal GMM fits, when available, are plotted over the histograms. The dashed line is a one-to-one line.

(iii) *Version 1.0 of unpublished Yonsei Evolutionary Population Synthesis (YEPS) models.* These models are described in Yoon et al. (2006, 2011). Created to study the integrated colours of GCs, these models assume a Salpeter (1955) IMF and provide both scaled solar and α element enhanced models. We used models with $[\alpha/\mathrm{Fe}] = 0.3$ and an age of 13 Gyr. Although these models predict realistic colours at intermediate metallicities, they predict colours that are too red at high and low metallicities.

(iv) *Version 2.3 of the Flexible Stellar Population Synthesis (FSPS) models of Conroy et al. (2009).* We used 12.6 Gyr models and a Kroupa (2001) IMF. The FSPS models show good agreement with observations at all metallicities except at the metal-rich end, where they are too red.

(v) *The Teramo Stellar Population Tools (SPoT) models of Raimondo et al. (2005).* These models were used in the Cantiello & Blakeslee (2007) and Blakeslee, Cantiello & Peng (2010) theoretical studies of GC bimodality. These models assume a Scalo (1998) IMF and we used their models with an age of 13 Gyr. We converted the $(V - I)$ colours provided by these models to $(g - i)$ using the transform of Jordi et al. (2006). These models only provide colours similar to observations at intermediate metallicities; at low and high metallicities the predicted colours are too red.

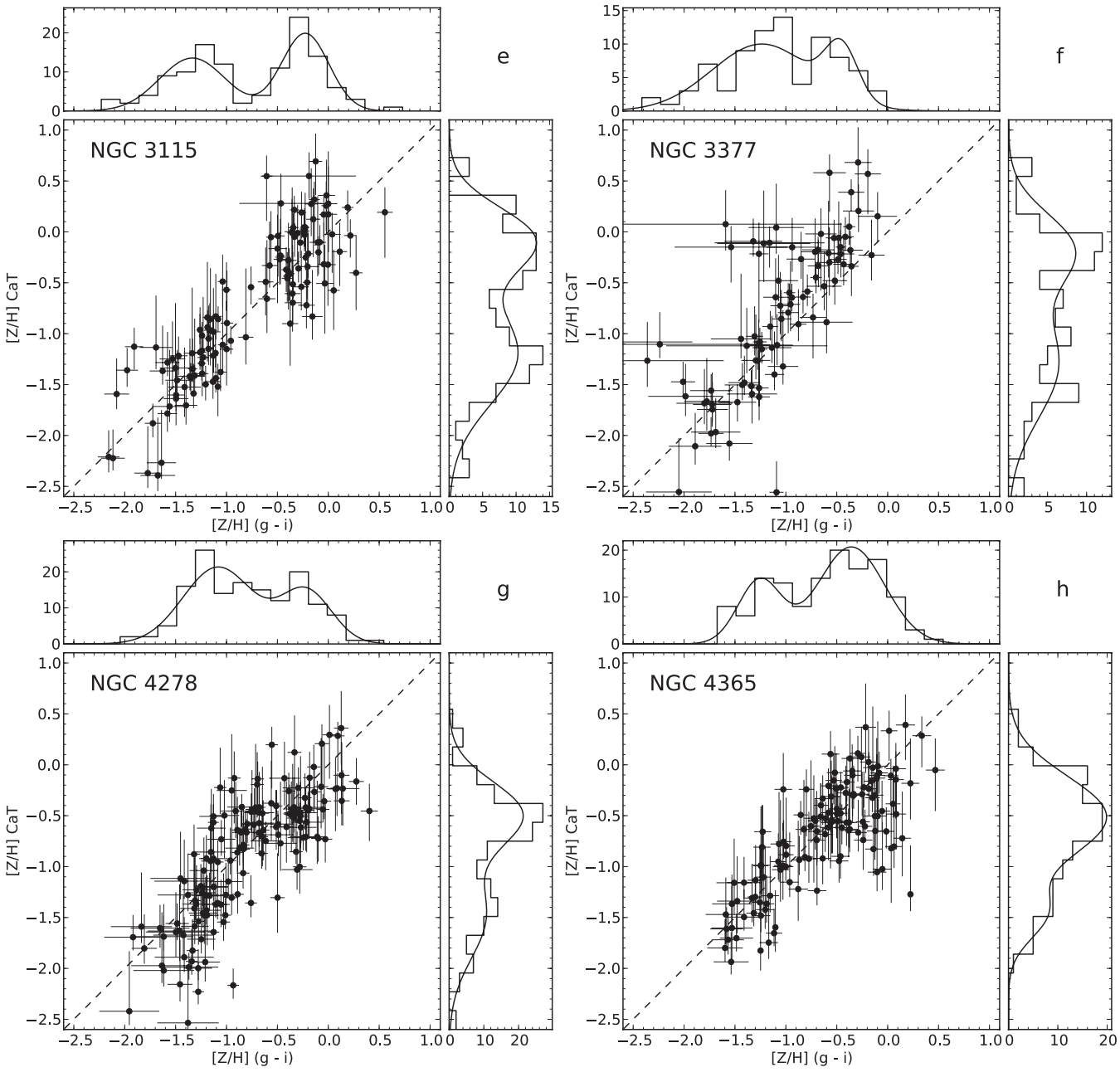

Figure 10 – *continued*

Since we compare models with different adopted IMFs, we used the Vazdekis et al. (2010) models to investigate the effects of varying the IMF on the colour–metallicity relation. Moving from a Kroupa (2001) IMF to a Scalo (1998) IMF caused the $(g - i)$ colour to become bluer but by less than 0.01 mag. Moving from a Kroupa (2001) IMF to a Salpeter (1955) IMF caused the $(g - i)$ colour to become redder by 0.03 mag with the shift being independent of metallicity. IMFs more bottom heavy than Salpeter (1955) have a larger redward shift. Similar results were seen with the FSPS models. We conclude that the colour–metallicity relation is almost identical for bottom light IMFs such as the Kroupa (2001) and the Scalo (1998) IMFs while bottom heavy IMFs such as the Salpeter (1955) IMF have redder colours. Therefore the SPoT models which use a Scalo (1998) IMF are directly comparable to the other models which use a Kroupa (2001) IMF, while the YEPS models are likely a few hundredths of a magnitude too red due to their choice of a Salpeter (1955) IMF.

All the models predict redder colours at the metal-rich end than are observed. It is unknown whether this is due to a failing of the colour–metallicity predictions of SSP models, due to an issue with the TMB03+TMK04 models used to derive the metallicities, or a mixture of the two. Out of the five SSP models we compare, the FSPS models of Conroy et al. (2009) appear to provide the closest match to observations. However, it is difficult to quantitatively show that one model agrees with observations better than the others due to similarities of the models and the limitations of our data.

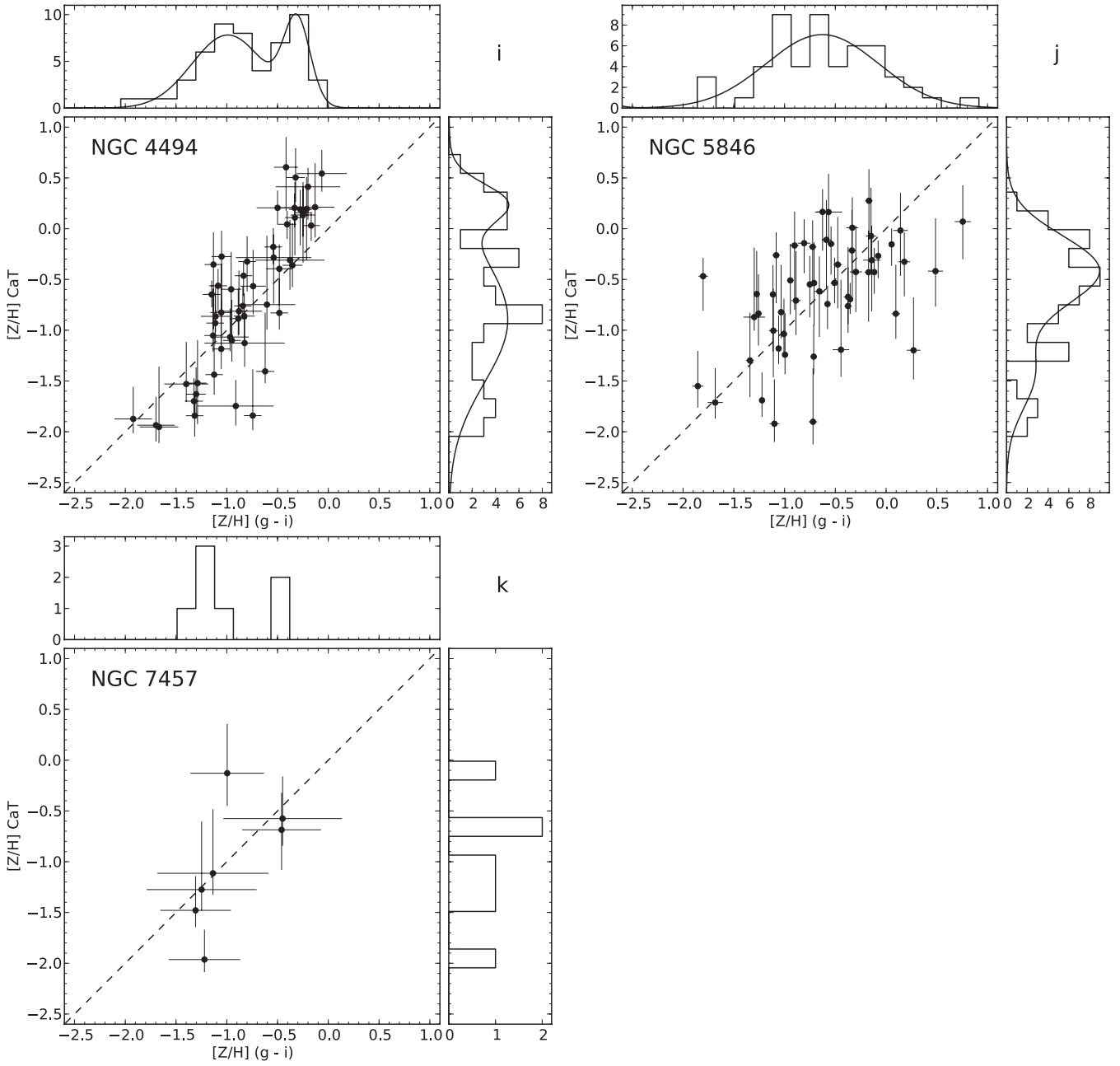

Figure 10 – *continued*

In five of our 11 galaxies (NGC 1400, NGC 1407, NGC 2768, NGC 3377 and NGC 4494) the KS test (Fig. 9) provides evidence that the CaT-based metallicities are not drawn from the same distribution as the colour-based metallicities, while in a sixth (NGC 4278) the KS test says there is a low but not significant probability that the two metallicities are not drawn from the same distribution. In the case of NGC 2768 the poor agreement between colour-based and CaT-based metallicity is likely due to the poor photometry available for this galaxy. The inner regions of NGC 3377 also suffer from poor photometry; however when GCs with poor photometry are removed, the disagreement between colour and CaT-based metallicity remains.

Although NGC 1407 shows good agreement at high metallicities it displays poor agreement at low metallicities with the colour-based metallicities being more metal-rich than the CaT-based metallicities (Figs 9c and 10c). NGC 1407's GCs possess a strong blue tilt (Harris et al. 2006), a colour–magnitude (mass–metallicity) relation where the colour (metallicity) peak of the blue (metal-poor) subpopulation becomes redder (more metal-rich) with brighter magnitudes (higher mass) (Mieske et al. 2006; Strader et al. 2006). The blue tilt is thought to have caused by GCs self-enrichment as more massive GCs are able to hold on to more of the metals formed by the first stars to form in the GCs (e.g. Bailin & Harris 2009). It is plausible that this self-enrichment changes the abundance pattern (e.g. the helium abundance) in such a way that the colour–metallicity relation (or at least the colour–CaT relation) is changed. The GCs we have CaT measurements for are affected by NGC 1407's blue tilt as can be seen in Fig. 1(c). NGC 4278 is possibly another example of this

effect as it also possesses a blue tilt (Usher et al., in preparation) and, like NGC 1407, shows weak evidence that the metal-poor GCs are redder than in other galaxies (Figs 9g and 10g).

Another possible explanation is that the metal-poor GCs in these galaxies have a different IMF than metal-rich GCs in these galaxies or all GCs in other galaxies. Using CaT SSP models of V03 and the colours from the SSP models of Vazdekis et al. (2010), we found that going from a Kroupa (2001) IMF to a Salpeter (1955) IMF increased the measured CaT metallicity by 0.02 dex but make the $(g - i)$ colour 0.03 mag redder which due to the steeper colour–metallicity relation would increase the metallicity derived from metallicity by 0.25 dex, while a bottom heavy IMF similar that found by van Dokkum & Conroy (2010) in the most massive ellipticals (slope $x = -3$) increased the measured CaT metallicity by 0.07 dex but would make the colour 0.12 mag redder which would increase the colour-based metallicity by 0.9 dex. Thus the redder colours of metal-poor GCs in NGC 1407 and NGC 4278 could be explained by a more bottom heavy IMF for these GCs than that of other GCs.

Both NGC 3377 and NGC 4494 show the opposite trend, with agreement at low metallicities and the colour-based metallicities giving lower values than the CaT-based ones at high metallicities (Figs 9f, i, 10f and i). In both NGC 3377 and NGC 4494 the relationship between colour and metallicity appears to be linear and to be steeper than in other galaxies. The bluer colours of metal-rich GCs in these galaxies could be explained by some of the metal-rich GCs being younger than in other galaxies. In FSPS models of Conroy et al. (2009), at solar metallicity the $(g - i)$ colour difference between a 7.9 Gyr model and a 13.3 Gyr model is 0.10. Since the star formation history of early-type galaxies is dependent on mass and environment (e.g. Trager et al. 2000; Terlevich & Forbes 2002; Caldwell, Rose & Concannon 2003; Nelan et al. 2005; Thomas et al. 2005; Smith et al. 2012), it is natural to expect GCs in galaxies of different masses and environments to have different age–metallicity relations. Some evidence of this is seen in the Milky Way where GCs associated with dwarf galaxies that have been accreted on to the Milky Way show a different, steeper age–metallicity relation than those thought to have formed within the Galaxy itself (Forbes & Bridges 2010; Dotter, Sarajedini & Anderson 2011). NGC 1400 is different again with agreement at low metallicities while having more metal-rich colour-based values than CaT values at high metallicities (Figs 9b and 10b).

As noted in Section 2.1, our photometry is heterogeneous. Different photometric zero-points could shift the colour–metallicity relation along the colour axis or change its slope. We assumed one extinction value for all GCs in each galaxy so any differential reddening or internal extinction could affect the colours of different GCs with in a galaxy to differing degrees. It is unclear whether our heterogeneous photometry is responsible for the different colour–metallicity relations seen in different galaxies in our sample. If the colour–metallicity relation does vary from galaxy to galaxy it could be caused by variations in the ages or other stellar population parameters such as the IMF of the GCs between galaxies.

5.3 Globular cluster metallicity distributions

Although spectroscopic studies tend to sample the colour distribution well they are inherently biased to brighter magnitudes. If the stellar populations of the brightest GCs are different from the majority, then using only the brightest GCs will give a biased result. The blue tilt causes the metallicity distribution of the brightest GCs to be more metal rich and less bimodal than the metallicity distribution of the fainter GCs. We also note that the larger relative errors and smaller numbers in spectroscopic studies can make identification of metallicity bimodality more difficult than finding colour bimodality in photometric studies.

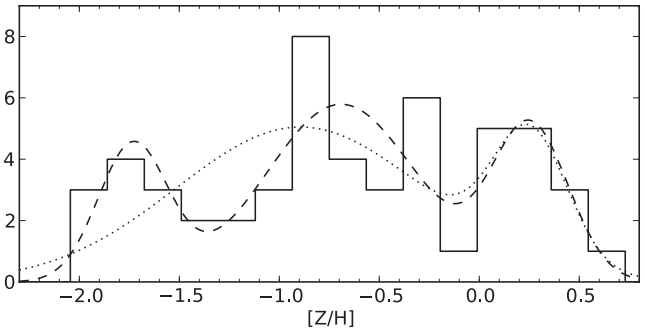

Figure 11. CaT metallicity distribution for NGC 4494. The solid line is a histogram of the measured metallicities. The dotted line is the two-peak GMM fit, while the dashed line is the three-peak GMM fit. GMM returns a higher probability that three Gaussians are preferred over one ($p = 0.90$) than two Gaussians ($p = 0.82$) are preferred over one. This hints that NGC 4494's metallicity distribution is trimodal rather than unimodal or bimodal.

Using GMM (Section 4.6, Table 4, Fig. 10), we detected CaT metallicity bimodality with a probability of greater than 0.95 in NGC 3115, NGC 4278 and NGC 4365 and greater than 0.90 in NGC 1407, NGC 5846 and NGC 3377. NGC 821, NGC 1400 and NGC 7457 do not have enough measured GCs to determine whether their distributions are bimodal or not. In NGC 2768 we do not see metallicity bimodality nor is the colour distribution of GCs with CaT measurements bimodal. Due to the poor quality of the photometry for this galaxy it is unclear whether we should expect metallicity bimodality.

NGC 4494 presents an interesting case. Although it does not meet one of our criteria for bimodality (a probability that two Gaussians are preferred over one of at least 0.9), GMM still gives a high probability that a two Gaussians are preferred over one of 0.819. The colour distribution of GCs with CaT measurements is bimodal (Table 5) so we would expect metallicity bimodality. Since the metallicity distribution of NGC 4494 appears trimodal (Fig. 11), we used GMM to test where the metallicity distribution is trimodal. We found peaks at [Z/H] $= -1.73 \pm 0.19$, -0.69 ± 0.14 and 0.26 ± 0.11, widths of 0.17 ± 0.12, 0.38 ± 0.12 and 0.19 ± 0.07, and 10.5 ± 5.8, 29.5 ± 7.7 and 13.0 ± 5.0 GCs in each peak. GMM gives a probability of 0.895 that a trimodal distribution is preferred over a unimodal distribution, a higher probability than for bimodal over unimodal. The peaks are well separated ($D = 3.55$ and 2.32) and the kurtosis is negative $k = -1.08$ supporting the existence of trimodality. The bimodal and trimodal GMM fits are plotted with the NGC 4494 metallicity histogram in Fig. 11. Due to the low number (53) of GCs these results should be treated with caution. F11 found evidence for three kinematic subpopulations in that although the bluest GCs and the reddest GCs in NGC 4494 show evidence for rotation, the intermediate colour GCs do not rotate. Taken together these lines of evidence suggest, but do not prove, that NGC 4494 has three GC subpopulations.

NGC 4365 shows evidence for colour trimodality (Blom et al. 2012b) and different kinematics for the different GC colour subpopulations (Blom et al. 2012a) so we also ran GMM with three peaks on this galaxy. Although GMM finds peaks at [Z/H] $= -1.53$, -0.70 and -0.20 which are located at the same places as the colour peaks found by Blom et al. (2012b) transformed into metallicity, GMM does

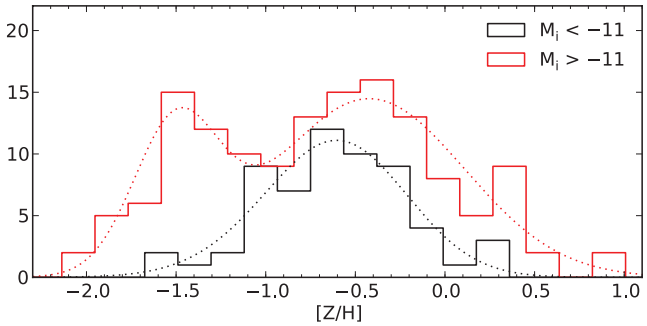

Figure 12. The CaT metallicity distribution of NGC 1407 split by magnitude. The black (red) histogram shows the distribution of GCs brighter (fainter) than $M_i = -11$, while the dotted lines give the GMM fits. For the bright GCs GMM gives a low probability that two Gaussians are preferred over one ($p = 0.014$), while for the faint GCs GMM gives a high probability ($p = 0.996$).

not find three Gaussians to be a significant improvement over one ($p = 0.671$). Due to the smaller numbers and larger errors of the CaT metallicities compared to the colours, it is not surprising that trimodality was not found to be an improvement.

In general the colour distributions of the GCs with CaT measurements are similar to the photometric GC candidate colour distribution in eight galaxies with sufficient numbers for GMM to be run. However, the blue peak of the GCs with CaT measurements in NGC 1407 is redder than the candidate blue peak in this galaxy due to the blue tilt while the red peak of the GCs in NGC 3377 is redder than that of the photometric GC candidates. The absolute magnitude limit of the GCs with CaT measurements varies dramatically as can be seen in the colour–magnitude diagrams in Fig. 1. In NGC 821, NGC 1400, NGC 1407 and NGC 5846, among the most distant galaxies in this study, the majority of GCs with CaT measurements are brighter than $M_i = -10$, while in NGC 3115 and NGC 3377, the closest galaxies, GCs as faint as $M_i = -8$ have CaT metallicities.

In Fig. 1(c) where the colour–magnitude and metallicity–magnitude diagrams of NGC 1407 are shown, the colour and metallicity distributions of GCs brighter than $M_i = -11$ appear different from those of fainter GCs. We split the GCs with CaT measurements in NGC 1407 into two magnitude bins and ran GMM on each. The results are plotted in Fig. 12. For GCs brighter than $M_i = -11$ the distribution looks quite unimodal. Fainter than $M_i = -11$ the distribution looks bimodal. GMM confirmed that this with the bright population showed a low probability that two Gaussians are preferred to one (0.014), while the faint population showed high probability that two Gaussians are preferred (0.996). If only the 100 brightest GCs in NGC 1407 had been studied spectroscopically bimodality would not have likely been found. This may explain why the Cohen et al. (1998) study of M87's GCs did not produce convincing proof of metallicity bimodality. It is known that in several galaxies including NGC 1407 (Romanowsky et al. 2009), M87 (Strader et al. 2011) and NGC 5128 (Woodley et al. 2010a), GCs brighter than $M_i \sim -11$ have different kinematics than fainter GCs further supporting the idea that the brightest GCs form a different population.

Out of the eight galaxies with significant numbers of GCs with CaT metallicity measurements, we see bimodality in six and evidence for trimodality in another. In the eighth galaxy we do not see multimodality. However, due to the poor quality of the photometry in this galaxy it is unclear whether we would expect bimodality based on the colour distribution of the observed GCs. Metallicity bimodality (or multimodality) appears to be a common feature in massive early-type galaxies.

5.4 Comparison with previous calcium triplet measurements

F10 used the CaT to measure the metallicity of 144 GCs in NGC 1407, while F11 used the same technique to measure the metallicity of 54 GCs in NGC 4494. In this study we have added additional GCs to the NGC 1407 data set and remeasured the CaT for all GCs in NGC 1407 and NGC 4494. Unlike the previous studies we normalized the continuum without human intervention (Section 3). Rather than calculate the uncertainty on the CaT measurements using the S/N as was done in F10 and F11, we used Monte Carlo resampling to calculate the errors which results in larger uncertainties. Unlike the earlier studies we corrected for an apparent S/N bias in the CaT index measurement (Section 4.2). We used a CaT metallicity calibration based on the SSP models of V03 rather than an empirical calibration based on the strength of the CaT in Milky Way GCs as measured by V03 (Section 4.4).

Despite the somewhat different analysis we get qualitatively similar results. The qualitative distributions of CaT indices in F10 and F11 both agree with this work, with NGC 1407 showing a bimodal distribution and NGC 4494 not showing clear bimodality. The shapes of the colour–CaT index relations we find are similar to those of the previous studies with NGC 1407 showing the relation steepening at low metallicities and NGC 4494 showing a linear relation.

In Fig. 13 we compare our measurements to those of F10 and F11. To be consistent with the calibration technique used in these papers we use the AZ88 metallicity calibration (equation 7), rather than the SSP model-based calibration (equation 8), for this comparison only. Additionally we use equation (6) in place of equation (2) of F10 to convert the CaT values of F10 and F11 into metallicities so any comparison is not biased by choice of metallicity scale. Although both measurements for NGC 1407 are consistent, for NGC 4494 we find that there is a significant offset with our measurements having metallicities 0.2 dex lower on average than those of F11.

Unlike F10 we do not see significant Paschen lines in any of our fitted NGC 1407 spectra. We note that the strength of the Paschen line index used increases with metallicity due to the presence of weak metal lines in the index passband so most of the higher Paschen index GCs tend to be high-metallicity GCs. Brodie et al. (2012) used SSP models to show that horizontal branch morphology has little effect on the strength of the CaT. Like F10 we find that the brightest GCs in NGC 1407 have similar CaT index values. However, we find that the colours of the brightest GCs when transformed into metallicity are also similar.

6 CONCLUSIONS

We have used the strength of the CaT to measure the metallicities of 903 GCs in 11 galaxies ranging from brightest group ellipticals to isolated lenticulars. This is the largest sample of spectroscopic GC metallicities ever assembled and the first to provide large numbers (>50) of metallicities for multiple galaxies. We showed that the CaT is a viable method of measuring the metallicity of extragalactic GCs with our CaT-derived metallicities agreeing with literature Lick index-based metallicities.

Using literature metallicities we defined a new colour–metallicity relation (equation 10). Although agreement is seen between the

metallicities predicted by this relation and CaT-based metallicities in half of our galaxies, the remaining galaxies show some disagreement either at low metallicity or at high metallicity. It is unclear whether these differences are caused by our heterogeneous photometry or real differences in the colour–metallicity relation between galaxies. Differences in the colour–metallicity relation could be driven by differences in the age or the IMF of GCs between galaxies.

We found spectroscopic metallicity bimodality in six of the eight galaxies with more than 40 GC measurements, while evidence of trimodality was seen in one of the remaining galaxies (NGC 4494) and we cannot rule out bimodality in the other (NGC 2768). We also found that the brightest GCs in NGC 1407 posses a different, unimodal metallicity distribution than the fainter, bimodal GCs. We caution that studies that rely on the properties of the brightest GCs to infer the properties of the GC system may give misleading results. These bimodality results are similar to what has been seen in previous spectroscopic studies of the GC metallicity distributions of early-type galaxies where three galaxies (NGC 5128, Beasley et al. 2008; NGC 4594, Alves-Brito et al. 2011; M49, Strader et al. 2007) show evidence of bimodality while the situation in a fourth galaxy (M87; Cohen et al. 1998) is inconclusive. When the previous studies are combined with our own results, nine of the 12 galaxies show evidence for bimodality while in the remaining three galaxies bimodality cannot be ruled out.

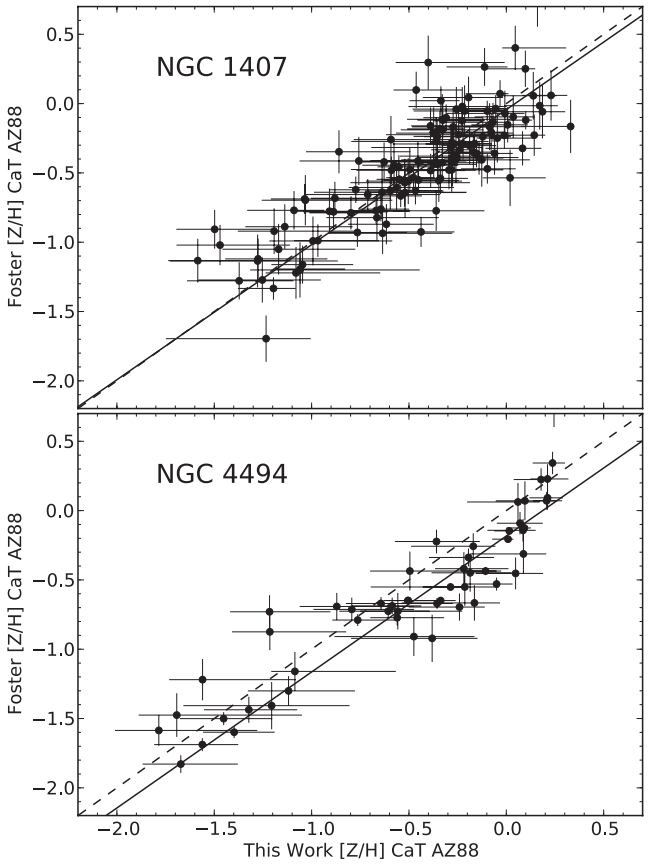

Figure 13. Top: comparison of CaT metallicities in NGC 1407 from Foster et al. (2010) with this work. Bottom: comparison of CaT metallicities in NGC 4494 from Foster et al. (2011) with this work. Overplotted with solid lines are linear fits to the metallicities, while the dashed line is one to one. Both studies give consistent metallicities for NGC 1407. While the slope is consistent with unity, the NGC 4494 metallicities are 0.2 dex lower than those of this work. For consistency we use the Armandroff & Zinn (1988)-based calibration (equation 7) rather than single stellar population model metallicity calibration (equation 8) used elsewhere in this work and convert the metallicities of Foster et al. (2010, 2011) to our metallicity scale.

The spatial distributions and kinematics of GCs system also favour multiple, distinct subpopulations. Red GCs are more centrally concentrated than blue GCs (e.g. Geisler, Lee & Kim 1996; Bassino, Richtler & Dirsch 2006; Harris 2009; Faifer et al. 2011; Forbes, Ponman & O'Sullivan 2012). In addition, the colour subpopulations often show different kinematics (Côté et al. 2003; Lee et al. 2010; Schuberth et al. 2010; Strader et al. 2011; Pota et al. 2012) with sharp changes in rotation occurring at the blue/red dividing line. NIR photometric studies (e.g. Kundu & Zepf 2007; Spitler et al. 2008b; Chies-Santos et al. 2012) also see evidence for bimodality in several galaxies although there are unresolved issues with the connection between metallicity and NIR photometry (Blakeslee et al. 2012).

Our observed GC metallicity distributions, together with other observations of GC systems, favour a picture where most massive galaxies have bimodal GC systems. Since GC metallicity bimodality appears to be common most early-type galaxies should have experienced two periods of intense star formation.

ACKNOWLEDGMENTS

We thank Karl Glazebrook, Lee Spitler and Albin Gaignette for providing data in advance of publication. We thank Michael Murphy, Vincenzo Pota and Christina Blom for valuable discussions and comments. We thank Mark Norris for assistance with the NGC 3115 Lick metallicities. We thank the anonymous referee for proving useful comments. This publication makes use of data products from the Two Micron All Sky Survey, which is a joint project of the University of Massachusetts and the Infrared Processing and Analysis Center/California Institute of Technology, funded by the National Aeronautics and Space Administration and the National Science Foundation. This research has made use of the NASA/IPAC Extragalactic Database (NED) which is operated by the Jet Propulsion Laboratory, California Institute of Technology, under contract with the National Aeronautics and Space Adminackistration. The analysis pipeline used to reduce the DEIMOS data was developed at UC Berkeley with support from NSF grant AST-0071048. This publication made use of PYRAF and PYFITS which are products of the Space Telescope Science Institute, which is operated by AURA for NASA. This research made use of TOPCAT (Taylor 2005). This research is partially based on data from the MILES project. Some of the data presented herein were obtained at the W. M. Keck Observatory, operated as a scientific partnership among the California Institute of Technology, the University of California and the National Aeronautics and Space Administration, and made possible by the generous financial support of the W. M. Keck Foundation. The authors wish to recognize and acknowledge the very significant cultural role and reverence that the summit of Mauna Kea has always had within the indigenous Hawaiian community. We are most fortunate to have the opportunity to conduct observations from this mountain. This research is based in part on data collected at Subaru Telescope, which is operated by the National Astronomical Observatory of Japan. This research is based on observations made with the NASA/ESA *Hubble Space Telescope*, obtained from the data archive at the Space Telescope Science Institute (STScI). STScI is operated by the Association of Universities for Research in Astronomy, Inc., under NASA contract NAS 5-26555. CF acknowledges co-funding under the Marie Curie Actions of the European

Commission (FP7-COFUND). This material is based upon work supported by the National Science Foundation under grants AST-0808099 and AST-0909237.

REFERENCES

Alves-Brito A., Hau G. K. T., Forbes D. A., Spitler L. R., Strader J., Brodie J. P., Rhode K. L., 2011, MNRAS, 417, 1823
Armandroff T. E., Zinn R., 1988, AJ, 96, 92 (AZ88)
Arnold J. A., Romanowsky A. J., Brodie J. P., Chomiuk L., Spitler L. R., Strader J., Benson A. J., Forbes D. A., 2011, ApJ, 736, L26
Ashman K. M., Bird C. M., Zepf S. E., 1994, AJ, 108, 2348
Bailin J., Harris W. E., 2009, ApJ, 695, 1082
Barmby P., Huchra J. P., Brodie J. P., Forbes D. A., Schroder L. L., Grillmair C. J., 2000, AJ, 119, 727
Bassino L. P., Richtler T., Dirsch B., 2006, MNRAS, 367, 156
Battaglia G., Irwin M., Tolstoy E., Hill V., Helmi A., Letarte B., Jablonka P., 2008, MNRAS, 383, 183
Beasley M. A., Bridges T., Peng E., Harris W. E., Harris G. L. H., Forbes D. A., Mackie G., 2008, MNRAS, 386, 1443
Blakeslee J. P., Cantiello M., Peng E. W., 2010, ApJ, 710, 51
Blakeslee J. P., Cho H., Peng E. W., Ferrarese L., Jordán A., Martel A. R., 2012, ApJ, 746, 88
Blom C., Forbes D. A., Brodie J. P., Foster C., Romanowsky A. J., Spitler L., Strader J., 2012a, MNRAS, preprint (arXiv:1207.6398)
Blom C., Spitler L. R., Forbes D. A., 2012b, MNRAS, 420, 37
Brodie J. P., Strader J., 2006, ARA&A, 44, 193
Brodie J. P., Strader J., Denicoló G., Beasley M. A., Cenarro A. J., Larsen S. S., Kuntschner H., Forbes D. A., 2005, AJ, 129, 2643
Brodie J. P., Usher C., Conroy C., Strader J., Arnold J. A., Forbes D. A., Romanowsky A. J., 2012, ApJ, submitted
Caldwell N., Rose J. A., Concannon K. D., 2003, AJ, 125, 2891
Caldwell N., Schiavon R., Morrison H., Rose J. A., Harding P., 2011, AJ, 141, 61
Cantiello M., Blakeslee J. P., 2007, ApJ, 669, 982
Cappellari M., Emsellem E., 2004, PASP, 116, 138
Cappellari M. et al., 2011, MNRAS, 413, 813
Cappellari M. et al., 2012, Nat, 484, 485
Carretta E., Gratton R. G., 1997, A&AS, 121, 95
Carretta E., Bragaglia A., Gratton R., D'Orazi V., Lucatello S., 2009, A&A, 508, 695
Cenarro A. J., Cardiel N., Gorgas J., Peletier R. F., Vazdekis A., Prada F., 2001, MNRAS, 326, 959
Cenarro A. J., Gorgas J., Cardiel N., Vazdekis A., Peletier R. F., 2002, MNRAS, 329, 863
Cenarro A. J., Beasley M. A., Strader J., Brodie J. P., Forbes D. A., 2007, AJ, 134, 391
Chies-Santos A. L., Larsen S. S., Cantiello M., Strader J., Kuntschner H., Wehner E. M., Brodie J. P., 2012, A&A, 539, A54
Chomiuk L., Strader J., Brodie J. P., 2008, AJ, 136, 234
Cohen J. G., Blakeslee J. P., Ryzhov A., 1998, ApJ, 496, 808
Cohen J. G., Blakeslee J. P., Côté P., 2003, ApJ, 592, 866
Conroy C., Gunn J. E., White M., 2009, ApJ, 699, 486
Cooper M. C., Newman J. A., Davis M., Finkbeiner D. P., Gerke B. F., 2012, in Astrophysics Source Code Library, record ascl:1203.003
Côté P., McLaughlin D. E., Cohen J. G., Blakeslee J. P., 2003, ApJ, 591, 850
Dotter A., Sarajedini A., Anderson J., 2011, ApJ, 738, 74
Faber S. M. et al., 2003, in Iye M., Moorwood A. F. M., eds, Proc. SPIE. Vol. 4841, Instrument Design and Performance for Optical/Infrared Ground-based Telescopes. SPIE, Bellingham, p. 1657
Faifer F. R. et al., 2011, MNRAS, 416, 155
Forbes D. A., Bridges T., 2010, MNRAS, 404, 1203
Forbes D. A., Brodie J. P., Huchra J., 1996, AJ, 112, 2448
Forbes D. A., Beasley M. A., Brodie J. P., Kissler-Patig M., 2001, ApJ, 563, L143
Forbes D. A., Sánchez-Blázquez P., Phan A. T. T., Brodie J. P., Strader J., Spitler L., 2006, MNRAS, 366, 1230
Forbes D. A., Ponman T., O'Sullivan E., 2012, MNRAS, preprint (arXiv:1205.5315)
Foster C., Forbes D. A., Proctor R. N., Strader J., Brodie J. P., Spitler L. R., 2010, AJ, 139, 1566 (F10)
Foster C. et al., 2011, MNRAS, 415, 3393 (F11)
Galleti S., Federici L., Bellazzini M., Buzzoni A., Pecci F. F., 2006, ApJ, 650, L107
Galleti S., Bellazzini M., Buzzoni A., Federici L., Fusi Pecci F., 2009, A&A, 508, 1285
Geisler D., Lee M. G., Kim E., 1996, AJ, 111, 1529
Girardi L., Bressan A., Bertelli G., Chiosi C., 2000, A&AS, 141, 371
Hargis J. R., Rhode K. L., Strader J., Brodie J. P., 2011, ApJ, 738, 113
Harris W. E., 1996, AJ, 112, 1487
Harris W. E., 2009, ApJ, 703, 939
Harris W. E., 2010, preprint (arXiv:1012.3224)
Harris W. E., Canterna R., 1979, ApJ, 231, L19
Harris W. E., Whitmore B. C., Karakla D., Okoń W., Baum W. A., Hanes D. A., Kavelaars J. J., 2006, ApJ, 636, 90
Jordi K., Grebel E. K., Ammon K., 2006, A&A, 460, 339
Kroupa P., 2001, MNRAS, 322, 231
Kundu A., Whitmore B. C., 2001, AJ, 121, 2950
Kundu A., Zepf S. E., 2007, ApJ, 660, L109
Kuntschner H., Ziegler B. L., Sharples R. M., Worthey G., Fricke K. J., 2002, A&A, 395, 761
Larsen S. S., Brodie J. P., Huchra J. P., Forbes D. A., Grillmair C. J., 2001, AJ, 121, 2974
Lee M. G., Park H. S., Hwang H. S., Arimoto N., Tamura N., Onodera M., 2010, ApJ, 709, 1083
Mackey A. D., Huxor A., Ferguson A. M. N., Tanvir N. R., Irwin M., Ibata R., Bridges T., Johnson R. A., Lewis G., 2007, ApJ, 655, L85
Maraston C., 2005, MNRAS, 362, 799
Mei S. et al., 2007, ApJ, 655, 144
Mendel J. T., Proctor R. N., Forbes D. A., 2007, MNRAS, 379, 1618
Merrett H. R. et al., 2003, MNRAS, 346, L62
Mieske S. et al., 2006, ApJ, 653, 193
Miyazaki S. et al., 2002, PASJ, 54, 833
Muratov A. L., Gnedin O. Y., 2010, ApJ, 718, 1266
Nelan J. E., Smith R. J., Hudson M. J., Wegner G. A., Lucey J. R., Moore S. A. W., Quinney S. J., Suntzeff N. B., 2005, ApJ, 632, 137
Newman J. A. et al., 2012, ApJS, preprint (arXiv:1203.3192)
Oke J. B. et al., 1995, PASP, 107, 375
Peacock M. B., Maccarone T. J., Knigge C., Kundu A., Waters C. Z., Zepf S. E., Zurek D. R., 2010, MNRAS, 402, 803
Peng E. W. et al., 2006, ApJ, 639, 95
Perina S., Federici L., Bellazzini M., Cacciari C., Fusi Pecci F., Galleti S., 2009, A&A, 507, 1375
Perina S., Galleti S., Fusi Pecci F., Bellazzini M., Federici L., Buzzoni A., 2011, A&A, 531, A155
Pota V. et al., 2012, MNRAS, submitted
Puzia T. H., Kissler-Patig M., Thomas D., Maraston C., Saglia R. P., Bender R., Goudfrooij P., Hempel M., 2005, A&A, 439, 997
Raimondo G., Brocato E., Cantiello M., Capaccioli M., 2005, AJ, 130, 2625
Rich R. M., Corsi C. E., Cacciari C., Federici L., Fusi Pecci F., Djorgovski S. G., Freedman W. L., 2005, AJ, 129, 2670
Richtler T., 2006, Bull. Astron. Soc. India, 34, 83
Romanowsky A. J., Strader J., Spitler L. R., Johnson R., Brodie J. P., Forbes D. A., Ponman T., 2009, AJ, 137, 4956
Rutledge G. A., Hesser J. E., Stetson P. B., 1997, PASP, 109, 907
Salpeter E. E., 1955, ApJ, 121, 161
Scalo J., 1998, in Gilmore G., Howell D., eds, ASP Conf. Ser. Vol. 142, The Stellar Initial Mass Function (38th Herstmonceux Conf.). Astron. Soc. Pac., San Francisco, p. 201
Schlegel D. J., Finkbeiner D. P., Davis M., 1998, ApJ, 500, 525
Schuberth Y., Richtler T., Hilker M., Dirsch B., Bassino L. P., Romanowsky A. J., Infante L., 2010, A&A, 513, A52

Sinnott B., Hou A., Anderson R., Harris W. E., Woodley K. A., 2010, AJ, 140, 2101
Skrutskie M. F. et al., 2006, AJ, 131, 1163
Smith R. J., Lucey J. R., Price J., Hudson M. J., Phillipps S., 2012, MNRAS, 419, 3167
Spitler L. R., Forbes D. A., Strader J., Brodie J. P., Gallagher J. S., 2008a, MNRAS, 385, 361
Spitler L. R., Forbes D. A., Beasley M. A., 2008b, MNRAS, 389, 1150
Spitler L. R., Romanowsky A. J., Diemand J., Strader J., Forbes D. A., Moore B., Brodie J. P., 2012, MNRAS, 423, 2177
Strader J., Brodie J. P., Cenarro A. J., Beasley M. A., Forbes D. A., 2005, AJ, 130, 1315
Strader J., Brodie J. P., Spitler L., Beasley M. A., 2006, AJ, 132, 2333
Strader J., Beasley M. A., Brodie J. P., 2007, AJ, 133, 2015
Strader J. et al., 2011, ApJS, 197, 33
Taylor M. B., 2005, in Shopbell P., Britton M., Ebert R., eds, ASP Conf. Ser. Vol. 347, Astronomical Data Analysis Software and Systems XIV. Astron. Soc. Pac., San Francisco, p. 29
Terlevich A. I., Forbes D. A., 2002, MNRAS, 330, 547
Thomas D., Maraston C., Bender R., 2003, MNRAS, 339, 897 (TMB03)
Thomas D., Maraston C., Korn A., 2004, MNRAS, 351, L19 (TMK04)
Thomas D., Maraston C., Bender R., Mendes de Oliveira C., 2005, ApJ, 621, 673
Tonry J. L., Dressler A., Blakeslee J. P., Ajhar E. A., Fletcher A. B., Luppino G. A., Metzger M. R., Moore C. B., 2001, ApJ, 546, 681
Trager S. C., Faber S. M., Worthey G., González J. J., 2000, AJ, 120, 165
van Dokkum P. G., Conroy C., 2010, Nat, 468, 940
Vazdekis A., Cenarro A. J., Gorgas J., Cardiel N., Peletier R. F., 2003, MNRAS, 340, 1317 (V03)
Vazdekis A., Sánchez-Blázquez P., Falcón-Barroso J., Cenarro A. J., Beasley M. A., Cardiel N., Gorgas J., Peletier R. F., 2010, MNRAS, 404, 1639
Villegas D. et al., 2010, ApJ, 717, 603
Woodley K. A., Gómez M., Harris W. E., Geisler D., Harris G. L. H., 2010a, AJ, 139, 1871
Woodley K. A., Harris W. E., Puzia T. H., Gómez M., Harris G. L. H., Geisler D., 2010b, ApJ, 708, 1335
Worthey G., 1994, ApJS, 95, 107
Worthey G., Faber S. M., Gonzalez J. J., Burstein D., 1994, ApJS, 94, 687
Yoon S., Yi S. K., Lee Y., 2006, Sci, 311, 1129
Yoon S.-J. et al., 2011, ApJ, 743, 150
Zinn R., 1985, ApJ, 293, 424
Zinn R., West M. J., 1984, ApJS, 55, 45

APPENDIX A: EMPIRICAL COLOUR TRANSFORMATIONS

For galaxies and GCs that lack *gri* imaging we used empirical colour conversions to give all GCs equivalent $(g - i)$ colours and i magnitudes. To convert *HST* ACS *gz* photometry into Suprime-Cam *gi* photometry, we derived the following relations using 169 spectroscopically confirmed GCs with both ACS and Suprime-Cam photometry in NGC 4365:

$$(g - i) = (0.735 \pm 0.009) \times (g - z) + (0.147 \pm 0.012)\,\mathrm{mag} \tag{A1}$$

and

$$i = z + (0.554 \pm 0.032) \times (g - z) + (-0.542 \pm 0.034)\,\mathrm{mag}. \tag{A2}$$

These relations were used to convert the ACS *gz* photometry in NGC 4278 and NGC 4365. We also used the same objects to derive a relation between $(g - r)$ and $(g - i)$:

$$(g - i) = (1.639 \pm 0.011) \times (g - r) + (-0.127 \pm 0.007)\,\mathrm{mag}. \tag{A3}$$

To convert $(V - I)$ colours into $(g - i)$ we derived the following relation using 30 photometric GC candidates in NGC 5846 brighter than $i = 23$:

$$(g - i) = (1.259 \pm 0.076) \times (V - I) - (0.411 \pm 0.069)\,\mathrm{mag}. \tag{A4}$$

To convert I to i we used the same data to get

$$i = I + (0.169 \pm 0.091) \times (V - I) + (0.143 \pm 0.099)\,\mathrm{mag}. \tag{A5}$$

We used these equations to convert the WFPC2 *VI* photometry in NGC 5846 and NGC 7457.

To convert *BI* photometry to *gi* we used the ACS *BI* photometry of Forbes et al. (2006) of NGC 1407 and 57 spectroscopically confirmed GCs in NGC 1407 to find

$$(g - i) = (0.651 \pm 0.015) \times (B - I) + (-0.187 \pm 0.025)\,\mathrm{mag} \tag{A6}$$

and

$$i = I + (0.162 \pm 0.146) \times (B - I) + (0.081 \pm 0.259)\,\mathrm{mag}. \tag{A7}$$

We used these relations to convert the ACS *BVI* photometry in NGC 2768. Using 30 spectroscopically confirmed GCs in NGC 2768 with both transformed ACS and Suprime-Cam photometry, we derived a relation between $(R - z)$ and $(g - i)$:

$$(g - i) = (0.913 \pm 0.227) \times (R - z) + (0.408 \pm 0.154)\,\mathrm{mag}. \tag{A8}$$

We used this relation to convert the colours of GCs with only *Riz* Suprime-Cam photometry in NGC 2768.

To convert *BVR* photometry into a *gi* photometry we used the Wisconsin Indiana Yale NOAO telescope (WIYN) Minimosaic *BVR* photometry of NGC 821 from Spitler et al. (2008a) together with 42 spectroscopically confirmed GCs to get the following:

$$(g - i) = (1.457 \pm 0.101) \times (B - R) + (-0.878 \pm 0.103)\,\mathrm{mag} \tag{A9}$$

and

$$i = R + (-0.565 \pm 0.086) \times (B - R) + (0.385 \pm 0.084)\,\mathrm{mag}. \tag{A10}$$

We used this to convert the WIYN Minimosaic *BVR* photometry of NGC 7457.

For NGC 4278 Pota et al. (2012) prefer ACS photometry to Suprime-Cam photometry. When ACS photometry is unavailable they convert the Suprime-Cam *BVI* photometry into *gz*. We used equations (A1) and (A2) to convert *gz* into *gi*.

APPENDIX B: EMPIRICAL COLOUR–METALLICITY RELATIONS

Using the preceding colour–colour relations we converted equation (10) into other optical colours:

$$[\mathrm{Z/H}] = \begin{cases} (5.47 \pm 0.94) \times (g - z) + (-5.95 \pm 1.02) \\ \qquad\qquad (g - z) < 0.84 \\ (2.56 \pm 0.09) \times (g - z) + (-3.50 \pm 0.11) \\ \qquad\qquad (g - z) > 0.84 \end{cases}, \tag{B1}$$

$$[\mathrm{Z/H}] = \begin{cases} (12.23 \pm 2.10) \times (g-r) + (-8.04 \pm 1.01) \\ \qquad\qquad (g-r) < 0.55 \\ (5.72 \pm 0.20) \times (g-r) + (-4.47 \pm 0.11) \\ \qquad\qquad (g-r) > 0.55 \end{cases}, \quad \text{(B2)}$$

$$[\mathrm{Z/H}] = \begin{cases} (9.36 \pm 1.71) \times (V-I) + (-0.16 \pm 1.24) \\ \qquad\qquad (V-I) < 0.94 \\ (4.39 \pm 0.30) \times (V-I) + (-5.46 \pm 0.27) \\ \qquad\qquad (V-I) > 0.94 \end{cases}, \quad \text{(B3)}$$

$$[\mathrm{Z/H}] = \begin{cases} (4.86 \pm 0.84) \times (B-I) + (-8.48 \pm 1.04) \\ \qquad\qquad (B-I) < 1.47 \\ (2.27 \pm 0.09) \times (B-I) + (-4.68 \pm 0.14) \\ \qquad\qquad (B-I) > 1.47 \end{cases}. \quad \text{(B4)}$$

SUPPORTING INFORMATION

Additional Supporting Information may be found in the online version of this article:

Table 3. Calcium triplet measurements and metallicities.

Please note: Wiley-Blackwell are not responsible for the content or functionality of any supporting materials supplied by the authors. Any queries (other than missing material) should be directed to the corresponding author for the article.

This paper has been typeset from a TEX/LATEX file prepared by the author.